REVISION 2

Ferropyrosmalite-bearing fluid inclusions in the North Patagonian Andes metasedimentary basement, Argentina: A record of regional metasomatism

Graciela Sosa[1], Sebastián Oriolo[2]*, Alfons Van den Kerkhof[l], Pablo Diego González[3], Ezequiel Olaizola[4], Florencia Bechis[4]

[1] Geoscience Center, Georg-August-Universität Göttingen, Goldschmidtstrasse 3, D-37077 Göttingen, Germany.

[2] CONICET-Universidad de Buenos Aires. Instituto de Geociencias Básicas, Aplicadas y Ambientales de Buenos Aires (IGEBA), Intendente Güiraldes 2160, C1428EHA Buenos Aires, Argentina.

[3] Instituto de Investigación en Paleobiología y Geología (UNRN-CONICET), Avenida Julio A. Roca 1242, R8332EXZ General Roca, Argentina.

[4] Instituto de Investigaciones en Diversidad Cultural y Procesos de Cambio, CONICET-Universidad Nacional de Río Negro, Bartolomé Mitre 630, R8400AHN San Carlos de Bariloche, Argentina.

*Corresponding author: seba.oriolo@gmail.com, soriolo@gl.fcen.uba.ar

Abstract

Quartz segregations in paragneisses from the Paleozoic basement of the North Patagonian Andes contain highly saline multiphase fluid inclusions with the rare daughter mineral ferropyrosmalite detected by Raman analysis, besides halite, sylvite, hematite and/or magnetite. During heating experiments, L-V homogenization occurs (256-515 °C), followed by halite dissolution (287-556 °C) and the dissolution of ferropyrosmalite at 550-581 °C. The latter phase transition triggers the growth of clino-amphibole crystals according to the following idealized reactions, written for potential end-members:

This is the peer-reviewed, final accepted version for American Mineralogist, published by the Mineralogical Society of America.
The published version is subject to change. Cite as Authors (Year) Title. American Mineralogist, in press.
DOI: https://doi.org/10.2138/am-2021-7525. http://www.minsocam.org/

$$4Fe_8Si_6O_{15}[(OH)_6Cl_4] + 6Ca^{2+}\ (aq.) \leftrightarrow 3Ca_2Fe_5Si_8O_{22}(OH)_2 + 17Fe^{2+}\ (aq.) + 16\ Cl^-\ (aq.) + 12OH^- + 3H_2$$

Ferropyrosmalite ↔ *Ferro-actinolite*

$$Fe_8Si_6O_{15}[(OH)_6Cl_4] + 2Ca^{2+}\ (aq.) + Fe^{+3}\ (aq.) + 2Al^{3+}\ (aq.) + Na^+\ (aq.) + H_2O \leftrightarrow NaCa_2(Fe^{2+}{}_4Fe^{3+})(Al_2Si_6)O_{22}Cl_2 + 4Fe^{2+}\ (aq.) + 2Cl^-\ (aq.) + 4H_2$$

Ferropyrosmalite ↔ *Chloro-hastingsite*

The amphibole resembles the composition of ferro-actinolite but has also striking similarities with chloro-hastingsite, as indicated by Raman spectroscopy. During the heating experiment, hematite (when present) transforms to magnetite by the uptake of H_2, whereas inclusions without Fe-oxides contain traces of H_2 after the reaction. This mineral transformation shows that ferropyrosmalite might result from the retrograde reequilibration of amphibole with the brine, implying the uptake of Fe^{2+}, Cl^- and H_2O, and the enrichment of Ca^{2+} in the brine. Pervasive fluid flow and fluid-assisted diffusion are recorded by channelway microstructures, healed microfractures and dissolution-reprecipitation phenomena, as demonstrated by cathodoluminescence microscopy. These alkali- and $FeCl_2$-rich brines, derived from magmatic sources and of possible Mesozoic age, were related to regional metasomatism, coeval with widespread granitoid activity.

Keywords: Ferropyrosmalite, ferro-actinolite, chloro-hastingsite, fluid inclusions, Raman spectroscopy, fluid-assisted diffusion

52

53 ## Introduction

54 Metasomatism is a solid-state metamorphic process that implies changes in the bulk
55 composition, mineralogy and microstructures of rocks due to fluid-rock interaction
56 (Zharikov et al. 2007; Harlov and Austrheim 2012). In the continental crust, metasomatic
57 fluids are commonly derived from magmas and sedimentary brines, though they may have
58 a metamorphic or mantle origin as well (Yardley and Bodnar 2014). Fluids may not only
59 act as merely catalysts, but also cause compositional changes, introducing dramatic
60 modifications to thermodynamic conditions (e.g., Putnis 2009; Putnis and Austrheim 2010;
61 Putnis and John 2010). In addition, fluid-assisted diffusion can induce reequilibration
62 through dissolution of parent phases and reprecipitation of products, producing mineral
63 replacement. Coupled dissolution-reprecipitation is thus the main mechanism for mineral
64 replacement reactions related to metasomatism (Putnis and Austrheim 2010; Ruiz-Agudo et
65 al. 2014).

66 Fluid inclusions represent an irreplaceable tool for monitoring fluid flow associated
67 with metasomatic processes (e.g., Kwak 1986; Harlov and Austrheim 2012; Raič et al.
68 2018). In high- to medium-grade metamorphic rocks, metasomatism commonly occurs
69 during retrograde metamorphism and associated hydrothermal processes, triggering post-
70 entrapment reequilibration of fluid inclusions that may significantly replace the primary
71 peak metamorphic assemblage (Vityk and Bodnar 1995; Touret 2001; van den Kerkhof et
72 al. 2014; Bakker 2017). Such complex histories can only be disentangled by a careful
73 examination of fluid inclusion microthermometric data in the light of microstructures based
74 on both petrographic and cathodoluminescence (CL) observations, which can be further

complemented by compositional data obtained by Raman spectroscopy, electron microprobe (EMP) or laser ablation – inductively coupled plasma – mass spectrometry (LA-ICP-MS) techniques (e.g., Touret 2001; van den Kerkhof and Hein 2001; Frezzotti et al. 2012; van den Kerkhof et al. 2014; Wagner et al. 2016).

Ferropyrosmalite, the Fe-rich end-member of the pyrosmalite series [$(Fe,Mn)_8Si_6O_{15}(OH,Cl)_{10}$; Yang et al. 2012], is a relatively rare phyllosilicate that occurs in different metal-bearing ore deposits and is intimately associated with metasomatic processes, mostly attributed to the presence of hypersaline hydrothermal fluids (Li and Naldrett 1993; Pan et al. 1993; Borrok et al. 1998; Tazava et al. 1999; Hanley and Mungall 2003; Cepedal et al. 2003; Koděra et al. 2003; Wanhainen et al. 2012). Though commonly associated with actinolite, sulphides, chlorides and iron oxides (Vaughan 1986; Pan et al. 1993; Dong and Pollard 1997; Koděra et al. 1998; Tazava et al. 1999; Hanley and Mungall 2003), robust constraints on ferropyrosmalite genetic conditions are still scarce. In this context, Koděra et al. (2003) proposed a retrograde reaction of clinopyroxene to ferropyrosmalite in saline fluid inclusions from altered granodiorites associated with a Fe-skarn deposit. Since the reaction between both minerals occurs at ca. 450 °C, clinopyroxene might have been originally present as a daughter mineral, but was subsequently replaced by ferropyrosmalite as part of a low-temperature equilibrium assemblage (Koděra et al. 2003).

The aim of this paper is thus to evaluate post-metamorphic metasomatic processes recorded by the Late Paleozoic metamorphic basement exposed in northwestern Patagonia, providing new insights into ferropyrosmalite genesis and equilibrium conditions. For this purpose, a detailed study was carried out in fluid inclusions from metamorphic quartz segregations of high- to medium-grade metasedimentary rocks, combining fluid inclusion

98 petrography, cathodoluminescence, microthermometry and Raman spectroscopy. Results
99 are finally discussed in the context of regional tectonometamorphic and magmatic
100 processes.

101

102 **Geological setting**

103 The North Patagonian Andes south of the Nahuel Huapi lake include basement
104 rocks that comprise paragneisses and schists with subordinate intercalations of
105 amphibolites, metarhyolites, felsic orthogneisses and foliated intrusions (Fig. 1; Dalla Salda
106 et al. 1991; García-Sansegundo et al. 2011; Oriolo et al. 2019). Though classically
107 attributed to the Colohuincul Complex (Dalla Salda et al. 1991), these rocks were recently
108 redefined as part of the Bariloche Complex (Oriolo et al. 2019), mostly due to differences
109 in the age of the protolith deposition and the timing and characteristics of metamorphism
110 and deformation. Devonian to Carboniferous metamorphism and deformation are
111 constrained by monazite EPMA Th-U-Pb ages of 391.7 ± 4.0 and 350.4 ± 5.8 Ma for
112 migmatitic paragneisses near the Brazo Tronador (Martínez et al. 2012), and monazite
113 EPMA Th-U-Pb ages of 299 ± 8 and 302 ± 16 Ma for garnet-bearing schists of the
114 Challhuaco hill (Oriolo et al. 2019).

115 Jurassic granitoids intruding the basement yield zircon U-Pb SHRIMP
116 crystallization ages of ca. 176-160 Ma (Castro et al. 2011a). Coeval low-grade
117 metamorphism and deformation of the basement was indicated by Oriolo et al. (2019)
118 based on monazite EPMA Th-U-Pb ages of 171 ± 9 and 170 ± 7 Ma. In addition, scarce
119 Late Jurassic volcano-sedimentary rocks are also exposed (Giacosa et al. 2001). Cretaceous

120 granitoids may be present as well, as suggested by K-Ar and Rb-Sr ages of ca. 120-80 Ma
121 (González Díaz 1982 and references therein). Despite the fact that monazite EPMA Th-U-
122 Pb ages of 110 ± 10 and 80 ± 20 Ma recorded by basement rocks suggest the presence of
123 Cretaceous magmatism and associated hydrothermal processes, the interpretation of these
124 ages is still unclear (Oriolo et al. 2019). Finally, Cenozoic volcano-sedimentary sequences
125 and granites are exposed as well (González Díaz 1982; Rapela et al. 1988; Giacosa et al.
126 2001; Bechis et al. 2014).

127

128 ## Materials and methods

129 ### *Sampling and microstructural characterization*

130 Samples of quartz segregations were collected from paragneisses of the Bariloche
131 Complex for fluid inclusion analysis. Quartz segregations are parallel to the ubiquitous S_2
132 metamorphic foliation, which represents the axial plane foliation of tight to isoclinal F_2
133 folds (Fig. 2a; García-Sansegundo et al. 2009; Oriolo et al. 2019). Rootless hinges of F_2
134 folds are commonly defined by folded quartz segregations (Fig. 2b; Oriolo et al. 2019).
135 Samples were collected from paragneisses exposed at the western margin of the Jakob lake
136 (sample BA 6-18; 41°11'03.1''S, 71°34'20.8''W) and the López hill (sample BA 28-18;
137 41°06'09.7''S, 71°33'40.8''W) (Fig. 1).

138 Due to the presence of relicts of folded S_1 in the microlithons of S_2, the latter is
139 observed as a crenulation schistosity, comprising mica domains and microlithons of quartz
140 and plagioclase (Oriolo et al. 2019). Plagioclase and garnet porphyroblasts are occasionally
141 present as well. Lepidoblastic muscovite and biotite exhibit shape-preferred orientation

This is the peer-reviewed, final accepted version for American Mineralogist, published by the Mineralogical Society of America.
The published version is subject to change. Cite as Authors (Year) Title. American Mineralogist, in press.
DOI: https://doi.org/10.2138/am-2021-7525. http://www.minsocam.org/

parallel to S_1 and S_2 planes, whereas quartz shows granoblastic microstructures. Fine-grained chlorite ± white mica ± opaque minerals are typical retrograde minerals that commonly exhibit shape-preferred orientation parallel to S_2 planes (Fig. 2c), which is locally affected by crenulation and F_3 microkinking (Oriolo et al. 2019). In addition, S_2 is cross-cut by fine-grained aggregates of epidote, chlorite, white mica, titanite, apatite and opaque phases (pyrite, chalcopyrite, magnetite and hematite), which overprint all aforementioned microstructural features. In few cases, decussate actinolite is present as well (Fig. 2d).

Methodology

Cathodoluminescence studies were carried out using a hot cathode HC3-LM-Simon-Neuser CL microscope (Neuser et al. 1995) equipped with a Kappa DX 40C Peltier-cooled camera. The operating conditions were 14 kV acceleration voltage and a beam current of < 1 mA, corresponding to 20-40 $\mu A/mm^2$ beam current density.

Phase transitions in fluid inclusions in quartz were investigated by using a LINKAM THMS 600 heating-freezing stage cooled with liquid nitrogen. The stage was calibrated by a set of synthetic fluid-inclusion standards. For temperatures around -56.6 °C (the melting point of CO_2) and around 0 °C, the accuracy is better than 0.5 °C, whereas for temperatures between 200 and 600 °C, the accuracy is better than 5 °C. Salinities of the brines were calculated from ice melting temperatures using the equations of Bodnar (2003), whereas the total salinities for oversaturated salt-bearing inclusions were estimated from the model of Steele-MacInnis et al. (2011).

This is the peer-reviewed, final accepted version for American Mineralogist, published by the Mineralogical Society of America.
The published version is subject to change. Cite as Authors (Year) Title. American Mineralogist, in press.
DOI: https://doi.org/10.2138/am-2021-7525. http://www.minsocam.org/

Raman analyses were accomplished in selected fluid inclusions using a Horiba-Jobin-Yvon HR-Raman spectrometer equipped with a 488 nm (blue) laser, attached to an Olympus BX41 microscope. For quantitative measurements, spectra were acquired using a 100x objective between 100 cm^{-1} and 4000 cm^{-1}, integrating 3 cycles of 30 s for each measurement. Measurements were mostly carried out in unpolarized mode, though polarized mode was also used in some cases, in order to check the effect of crystallographic orientation. Gas components were detected based on the Raman vibration bands for CO_2 (ca. 1388, 1285 cm^{-1}), N_2 (ca. 2930 cm^{-1}), H_2S (ca. 2611 cm^{-1}) and H_2 (ca. 4156 cm^{-1}), whereas gas ratios were determined with respect to the wavelength-dependent relative Raman scattering cross-sections for a 488 nm laser unit (Burke 2001).

Results

Cathodoluminescence of quartz

CL microscopy is a highly sensitive method for demonstrating or semi-quantifying rock alteration and paleo-porosity (e.g., Behr and Frentzel-Beyme 1987; Van den Kerkhof and Hein 2001). Under CL, the quartz in the microlithons shows initial bright blue colors, almost immediately changing to violet and red as a response to electron beam irradiation. A number of microstructures visible only under CL are indicative of fluid-rock interaction, including secondary zoning, grain boundary alteration, and channelway and cataclastic healed microstructures (Fig. 3). In the studied samples, microstructures associated with stages of high-temperature and low-temperature alteration were distinguished.

This is the peer-reviewed, final accepted version for American Mineralogist, published by the Mineralogical Society of America.
The published version is subject to change. Cite as Authors (Year) Title. American Mineralogist, in press.
DOI: https://doi.org/10.2138/am-2021-7525. http://www.minsocam.org/

Quartz shows secondary zoning characterized by diffusive compositional variations within quartz grains. These microstructures are particularly common in the samples from the López hill, which record higher metamorphic temperatures. The altered quartz shows typically red CL, whereas the remaining relic patchy quartz shows bluish CL (1 in Fig. 3a). The microstructures typically show convex forms, indicative of grain boundary diffusion of trace elements (Van den Kerkhof et al. 2004).

Low-temperature metasomatism is characterized by cataclastic textures (i.e., healed microfractures and channelway microstructures) and grain boundary diffusion showing initial dark CL, changing to bright brown and red during the measurements. Quartz grains typically show reduced CL intensity along the boundaries (2 in Figs. 3a, b), suggesting trace element depletion along the rims during pervasive fluid flow. Cross-cutting relationships show that the oldest fluid pathways show blue CL, whereas younger microstructures show brown CL (3 and 4 in Fig. 3b). At the López hill, the blue CL in the channelways suggests the interaction with hot circulating fluids, whereas the latter microstructures are associated with alteration minerals like chlorite, epidote and apatite in veins and nests.

Quartz from the Jakob lake locality shows a dominance of low-temperature features. Quartz with extensive cataclastic microstructures exhibits unstable blue CL (5 in Fig. 3c), which grade to final bright red CL during electron beam irradiation. More complex microstructures (bright red CL) are related to subgrains, which are indicative of local recrystallization (6 in Fig. 3c).

This is the peer-reviewed, final accepted version for American Mineralogist, published by the Mineralogical Society of America.
The published version is subject to change. Cite as Authors (Year) Title. American Mineralogist, in press.
DOI: https://doi.org/10.2138/am-2021-7525. http://www.minsocam.org/

Fluid inclusions

Fluid inclusions from the López hill location were studied in the mirrored fluid plates of the CL sections, whereas those from the Jakob lake location were poorly preserved and could not be measured by microthermometry. Based on fluid phase petrography, early secondary multiphase inclusions and late secondary two-phase inclusions were identified (Table 1).

Abundant multiphase highly saline fluid inclusions occur in clusters or are isolated, and can be classified as early secondary, i.e., inclusions trapped during metasomatic overprint and linked with the earliest fluid pathways in CL. They typically contain liquid and vapor with a wide range of water volume fractions (0.10-0.65) together with several solid phases. The latter may take up to 70 vol. % of the inclusions (Table 1). Halite and sylvite are common daughter phases together with a number of Raman-active crystals. Sylvite crystals, sometimes absent, are always smaller than halite. Rare early secondary two-phase inclusions also occur, showing lower water volume fractions of 0.30-0.40 and sometimes salt crystals (halite or halite + sylvite). The Raman-active minerals could be identified as ferropyrosmalite and hematite (Fig. 4), or sometimes magnetite. The unusual mineral ferropyrosmalite was optically observed as a transparent, colorless crystal with occasional hexagonal morphology, which is in accordance with its trigonal symmetry (Fig. 4a). The bubble normally contains no detectable gas, but occasionally traces of CO_2 occur, as revealed by Raman analysis. Eutectic melting was normally observed between -58 and -54 °C, indicating the presence of significant Ca^{2+} (± Fe^{2+}, Mg^{2+}) concentrations in the brine. After subsequent heating, the melting of ice between -46 and -28 °C, followed by the melting of hydrohalite between -20 and -12 °C, was typically observed. During heating

This is the peer-reviewed, final accepted version for American Mineralogist, published by the Mineralogical Society of America.
The published version is subject to change. Cite as Authors (Year) Title. American Mineralogist, in press.
DOI: https://doi.org/10.2138/am-2021-7525. http://www.minsocam.org/

experiments, LV-homogenization of the early secondary multiphase inclusions took place between 256 and 515 °C (Fig. 5a). Sylvite, if present, always dissolves before halite at ca. 190 °C. However, NaCl must be dominant over KCl, since hydrohalite can be clearly identified. Halite dissolves always after L-V homogenization between 287 and 556 °C and shortly after ferropyrosmalite dissolves. It is immediately followed by the simultaneous growth of a new greenish mineral between 550 and 581 °C (Fig. 5b). In a temperature range of ca. 10-20 °C, both ferropyrosmalite and the new mineral coexist in the fluid inclusion. The new mineral often growths from the inclusion wall inwards and sometimes more than one crystal of the same species crystallizes within the same inclusion. This mineral was identified by Raman analysis as clino-amphibole (Fig. 4c). As a result of heating, several inclusions, notably those without an opaque phase, contain detectable amounts of H_2, as revealed by the appearance of a Raman peak at 4156 cm^{-1} (Burke 2001). Phase transition temperatures and fluid properties are summarized in Table 1 and Figure 5.

Salinity calculations for the brine estimated from ice melting temperatures with the equation of Bodnar (2003) yielded 27-33 wt. % NaCl eq. (Figs. 5c, 6). However, the eutectic temperatures of -58 to -54 °C, which mark the melting of antarcticite, indicate a $CaCl_2$-dominated brine with additional components, most likely NaCl and KCl, and probably more salts. As an approximation, brines are considered as ternary mixtures in the system H_2O-$CaCl_2$-NaCl. In that way, total salinity can be estimated from ice, hydrohalite and halite melting temperatures and the model of Steel-McInnes et al. (2011), yielding total salinity of 27-73 wt. % NaCl eq. (Figs. 5c, 6). The effect of additional KCl on the topology and isotherms in the ternary system, notably on the hydrohalite melting, is assumed to be minor, when considering the sum of dissolved alkali chlorides (Assarsson 1950). Ice melts

253 between -46 and -28 °C, and hydrohalite between -20 and -12 °C. For the oversaturated
254 multiphase inclusions, ice melting is often metastable, because halite is still present,
255 although salt hydrates and ice are the stable phases. However, the hydration reaction halite
256 to hydrohalite is very sluggish and does not occur here. On the other hand, L-V
257 homogenization and halite melting can be accurately reproduced in the heated inclusions,
258 returning the same phase transition temperatures documented before the reaction.

259 In the early secondary inclusions, the extreme variation in salinity may either result
260 from the simultaneous entrapment of fluid and halite or from different portions of the
261 evolving magmatic fluid (Fig. 5b). Because of halite crystallization, this may also explain
262 the clear trend of brine compositions between high-salinity NaCl-rich and low-salinity
263 $CaCl_2$-rich compositions (Fig. 6). The much lower solubility of NaCl compared to $CaCl_2$
264 ("salting out") results in the formation of halite crystals, which may become isolated in
265 modified inclusions. The rare and simpler early secondary inclusions without salts show the
266 same bulk compositions as the brine in the multiphase inclusions, pointing at incidental
267 fluid retrapping during cooling.

268 The late secondary inclusions are linked with the altered quartz showing brownish
269 and reddish CL. These inclusions are aligned along short trails and show variable H_2O
270 volume fractions, which fall in two groups: liquid-rich inclusions with water volume
271 fractions between 0.70 and 0.87, and vapor-rich inclusions with water volume fractions
272 between 0.05 and 0.30 (Table 1). The salinities of both inclusion types are generally low (<
273 5 wt. % NaCl), as deduced from ice melting temperatures (from -3.2 to 1.5 °C, for
274 metastable melting). The liquid-rich and vapor-rich inclusions occur in close association
275 within the same trails and were evidently trapped from immiscible fluids (heterogeneous

trapping) during cooling. Eutectic melting, if observed, shows temperatures around -21 °C, pointing at the dominance of NaCl in solution. Raman analysis shows that some V-L inclusions contain small amounts of CO_2, sometimes with traces of N_2 and/or H_2S. However, the rare observation of CO_2 or clathrate melting suggests very low density of the carbonic phase. This was confirmed by the properties of Raman spectra, pointing at densities <0.4 g/cm^3, i.e., always below the critical density of CO_2 (Fall et al. 2011), as the difference between the positions of the peaks of the Fermi diad is very small (between 102.4 and 103.5 cm^{-1}). Partial homogenization of the carbonic phases to vapor was not observed. Total homogenization temperatures of the vapor-rich inclusions (to the vapor phase) fall in a relatively narrow range between 319 and 389 °C. Homogenization temperatures of the liquid-rich inclusions (to the liquid phase between 254 and 384 °C) fall in the same range, but are in part lower (Fig. 5a).

Raman analysis of daughter phases

Ferropyrosmalite in multiphase brine inclusions was irrevocably identified by Raman analysis (Fig. 7a) with characteristic peaks at 614, 1024 cm^{-1}, and in the O-H stretching region at 3550, 3577 and 3626 cm^{-1} (Dong and Pollard 1997; Koděra et al. 2003). Some smaller peaks at lower wavenumbers were found at 190 and 324 cm^{-1}.

The opaque phase in the multiphase inclusions appeared to be either hematite (peaks at 223, 290, 403, 610 and 1305 cm^{-1}), or sometimes magnetite (peaks at 537 and 667 cm^{-1}). After heating of the inclusions, only magnetite could be detected when analyzing the opaque phases, suggesting hematite reduction.

This is the peer-reviewed, final accepted version for American Mineralogist, published by the Mineralogical Society of America.
The published version is subject to change. Cite as Authors (Year) Title. American Mineralogist, in press.
DOI: https://doi.org/10.2138/am-2021-7525. http://www.minsocam.org/

298 Heated brine inclusions contain clino-amphibole, as identified by Raman
299 spectroscopy (Fig. 7b). Strong Raman peaks were found in the 640-665 and 990-1015 cm^{-1}
300 ranges and relate to the amphibole chain structure (Lafuente et al. 2015). The peaks can be
301 assigned to the symmetrical and asymmetrical stretching vibrations of Si-O-Si bridges,
302 respectively. Smaller peaks at 250-400 and 500-550 cm^{-1} are probably associated with the
303 bending modes of the chains, as discussed by Apopei and Buzgari (2010). The same spectra
304 could be well-reproduced for ca. 10-15 crystals found in the heated sample. The
305 comparison with spectra of standard samples from the RRUFF database (Lafuente et al.
306 2015) shows similarities of the amphibole Raman spectra with ferro-actinolite (R060189)
307 as well as with hastingsite (R070194). One prismatic crystal of amphibole was measured in
308 polarized mode, parallel and perpendicular to the crystallographic c-axis (Fig. 7b).

309 Remarkable is the appearance of a clear Raman band at ca. 751-755 cm^{-1}, which
310 shows extreme intensity variation depending on the crystallographic orientation. In
311 polarized light, the intensity is strongest for vibrations perpendicular to the crystallographic
312 c-axis. The same peak was detected in reference samples of hastingsite (R070194) from the
313 RRUFF database (Lafuente et al. 2015) and amphiboles with $Fe^{3+}>^{[6]}Al^{3+}$ of
314 andesites/dacites from the Taapaco volcano, Chile (Banaszak 2014). Koděra et al. (2003)
315 noticed this peak for the new phase formed during heating and suggested the presence of
316 another unidentified mineral phase. However, the clear correlation with the other peaks
317 demonstrates that this Raman band must be part of the amphibole spectrum. In accordance
318 with the hastingsite spectra and findings of Leissner et al. (2015) and Roesche (2018) for
319 heated and oxidized amphiboles, it is assumed that the 751-755 cm^{-1} peak is associated with

trivalent iron, formed by the oxidation of divalent iron and resulting in the shift of the symmetrical stretching mode to higher wavenumbers.

The three peaks assigned to OH^- bonding, as recorded for ferropyrosmalite, disappeared after heating, or only one single peak in this range remained, which however does not coincide with any ferropyrosmalite peak. Several OH^- bonding peaks for amphibole fall in the 3570-3770 cm^{-1} range (Lafuente et al. 2015), but in the heated inclusions only two peaks, a larger at ca. 3619 cm^{-1} and a smaller one at ca. 3653 cm^{-1}, were detected for the majority of the ca. 10-15 analyzed inclusions. The low wavenumbers of these vibration modes can be explained by the substitution of Fe in the $M(1)O_6$-$M(1)O_6$-$M(3)O_6$ octahedra triplet sites and suggests a very high Fe/Mg ratio (Leissner et al. 2015; Roesche 2018). However, OH^- vibrational peaks were strongly reduced and, in 3-5 cases, are even absent. The lack of these vibration modes can be possibly explained by the substitution of OH^- by Cl^-, as indicated by Fornero et al. (2008). It has been reported that Fe-rich amphiboles contain high concentrations of chlorine (e.g., Volfinger et al. 1985; Rebay et al. 2015), though chlorine incorporation can be also controlled by the substitution of Al^{3+} for Si^{4+} at tetrahedral sites and K^+ for Na^+ at A sites (Jenkins 2019). As the Raman spectra of the amphiboles in the fluid inclusions suggest very high Fe-contents, it is thus expected that chlorine concentration may be relatively high as well. Note that the amphibole forms in oversaturated brines after the dissolution of halite, often with a sylvite crystal present. Therefore, the unusual Raman spectra for the newly formed amphibole best fits compositions rich in iron and in a state of high oxidation, also with a possible contribution of potassium.

This is the peer-reviewed, final accepted version for American Mineralogist, published by the Mineralogical Society of America.
The published version is subject to change. Cite as Authors (Year) Title. American Mineralogist, in press.
DOI: https://doi.org/10.2138/am-2021-7525. http://www.minsocam.org/

342 Finally, the bubbles of most natural, non-heated inclusions do not contain any
343 Raman-active gas components. Some inclusions, however, contain CO_2, sometimes with
344 subordinated N_2 and H_2S, with composition ca. $CO_2(83)N_2(12)H_2S(5)$ in the gas-rich late
345 secondary inclusions. In samples which formed amphibole on heating but do not contain
346 Fe-oxides, small amounts of H_2 could be detected as well.

347

348 ## Discussion

349 ### *Ferropyrosmalite genesis and mineral-brine reactions*

350 The association of ferropyrosmalite, halite, sylvite and Fe-oxide in more or less the
351 same volume ratios is typical for many of the studied fluid inclusions. Therefore, these
352 minerals are considered as true daughter phases and not as captive minerals. Another
353 argument is the absence of ferropyrosmalite as "solid inclusions" in quartz and exclusively
354 found associated with high-salinity brines. At ca. 600 °C (the maximum temperature which
355 can be reached with the heating stage), the clino-amphibole together with Fe-oxide, and
356 often also sylvite, persist and could not be dissolved during experiments. This implies that
357 inclusions must have formed at higher temperature, i.e., above the ferropyrosmalite-
358 amphibole equilibrium temperature, thus implying that ferropyrosmalite formed from a
359 retrograde reaction.

360 To our knowledge, the amphibole-forming reaction from ferropyrosmalite and brine
361 in the heated fluid inclusions is reported here for the first time. It is assumed that amphibole
362 must have been present in the inclusions at high temperatures and, consequently,
363 ferropyrosmalite formed because of retrograde reactions of this mineral with the brine. The

equilibrium temperature documented for the ferropyrosmalite to clino-amphibole reaction is 550-581 °C, which is more than 100 °C higher than the temperature reported by Koděra et al. (2003) for the ferropyrosmalite-hedenbergite reaction. In a similar way to the ferropyrosmalite–clino-amphibole transformation, the latter implies the uptake of $FeCl_2$ and H_2O, and the enrichment of Ca^{2+} in the brine (Koděra et al., 2003). Considering a pure Fe end-member for pyrosmalite, a pure ferro-actinolite amphibole, and that all released O_2 converts to OH^-, the equation for the ferropyrosmalite to amphibole transformation can be written as follows:

$$4Fe_8Si_6O_{15}[(OH)_6Cl_4] + 6Ca^{2+}\ (aq.) \leftrightarrow 3Ca_2Fe_5Si_8O_{22}(OH)_2 + 17Fe^{2+}\ (aq.) + 16\ Cl^-\ (aq.) + 12OH^- + 3H_2 \quad (1)$$

Ferropyrosmalite ↔ *Ferroactinolite*

On the other hand, assuming a pure Fe end-member for pyrosmalite and Cl-rich hastingsite, the following reaction would be plausible:

$$Fe_8Si_6O_{15}[(OH)_6Cl_4] + 2Ca^{2+}\ (aq.) + Fe^{+3}\ (aq.) + 2Al^{3+}\ (aq.) + Na^+\ (aq.) + H_2O \leftrightarrow NaCa_2(Fe^{2+}{}_4Fe^{3+})(Al_2Si_6)O_{22}Cl_2 + 4Fe^{2+}\ (aq.) + 2Cl^-\ (aq.) + 4H_2 \quad (2)$$

Ferropyrosmalite ↔ *Chloro-hastingsite*

As previously exposed, the amphibole shows similarities with ferro-actinolite and hastingsite, indicating a Fe-rich amphibole, most likely in a high oxidation state. The presence of Fe^{3+} is problematic for ferro-actinolite, which only contains Fe^{2+}, but could be satisfactorily explained by hastingsite. In that case, Raman evidence suggests a relatively

large Cl^-/OH^- ratio, pointing to a possible chloro-hastingsite composition, whereas the presence of K in A sites substituting K could also indicate potassic-chloro-hastingsite. The main limitation in the interpretation of hastingsite is the low solubility of Al^{3+}, which is expected together with ferropyrosmalite after the retrograde reaction (2).

At the same time, magnetite probably formed as the result of hematite reduction, according to the following reaction (Matthews 1976):

$$3Fe_2O_3 + H_2 \leftrightarrow 2Fe_3O_4 + H_2O \quad (3)$$

The source for the hydrogen for the reaction likely results from the breakdown of ferropyrosmalite, according to the amphibole-forming reactions (1) and (2).

The reactions take place essentially in a closed system without addition or loss of any components from the host mineral. The presence of significant amounts of Ca (±Fe, ±Mg) in the associated fluids is based on the recognition of antarcticite ($CaCl_2 \cdot 6H_2O$) in the inclusions during cooling-heating runs. Antarcticite melting at eutectic temperatures of ca. -55 °C was observed for the multiphase inclusions and point to NaCl-$CaCl_2$-bearing brines. Halite and sylvite reprecipitated on cooling and the newly formed phases seem to be stable at room temperature in most cases. The ferropyrosmalite-amphibole transformation appeared to be metastable over long periods, as the retrograde hydration-chlorination reaction to ferropyrosmalite has not been observed so far, not even after six hours of laser beam irradiation. However, Koděra et al. (2003) recorded the retrograde change from pyroxene to ferropyrosmalite, which was possibly stimulated by heating of the laser beam. Even though the retrograde reaction has not been observed under experimental conditions, it is assumed that it might have taken place in nature.

On the other hand, highest temperature conditions of > 581 °C recorded by fluid inclusions suggest the interaction of metasedimentary rocks with hot circulating fluids along channelways, presumably induced by post-peak metamorphic heating (e.g., van den Kerkhof et al. 2004). Such relatively high-temperature conditions are further supported by environmental conditions reported for the crystallization of Cl-rich amphiboles (e.g., Giesting and Filiberto, 2016, and references therein), assumed to be a primary phase in the studied fluid inclusions, and might be associated with regional low-pressure conditions, as indicated by geological evidence. The recorded evolution towards lower temperature fluids thus indicates a retrograde evolution from lower amphibolite to greenschist facies conditions. On the other hand, high salinity, Ca-Fe-rich fluids associated with ferropyrosmalite formation commonly have a magmatic source (e.g., Li and Naldrett 1993; Borrok et al. 1998; Tazava et al. 1999; Hanley and Mungall 2003; Koděra et al. 2003). The presence of magmatic sources for the studied fluids, possibly related to Mesozoic tectonomagmatic events, are further supported by microstructural and geochronological data of metamorphic rocks of the study area.

The existence of metasomatism coupled with regional retrograde conditions has deep implications for the study of metamorphic processes. In the first place, it poses a challenge for P-T thermodynamic modelling and construction of pseudosections, since the assumption of a closed system and isochemical conditions is not valid, as the protolith geochemical composition changes after interaction with the brine. On the other hand, no evidence of metasomatic processes during retrograde metamorphism had been recorded in the study area so far (García-Sansegundo et al. 2011; Martínez et al. 2012; Oriolo et al. 2019), whereas quartz segregations, which are structurally concordant with peak

metamorphic basement fabrics (Figs. 2a, b), do not show any macro-/microstructural evidence of a post-metamorphic overprint. Only the combined use of CL, fluid inclusion and Raman analyses revealed the complex metasomatic evolution of the system, emphasizing the role of fluid-assisted dissolution-reprecipation processes.

Regional implications

The Paleozoic basement of the North Patagonian Andes is affected by low-grade metamorphism and deformation (Oriolo et al. 2019) coeval with the intrusion of Jurassic granitoids at ca. 176-160 Ma (Castro et al. 2011a). This is indicated by monazite EPMA Th-U-Pb ages of 171 ± 9 and 170 ± 7 Ma, the latter recorded in the Jakob lake locality (Oriolo et al. 2019). On the other hand, minor monazite populations yielding ages of 110 ± 10 and 80 ± 20 Ma were also obtained in the Jakob lake and Challhuaco hill, respectively (Fig. 1; Oriolo et al. 2019). The presence of Cretaceous granitoids in the region, however, is only poorly constrained by K-Ar and Rb-Sr ages of ca. 120-80 Ma (González Díaz 1982 and references therein).

Based on P-T conditions for the monazite-allanite equilibrium, Oriolo et al. (2019) suggested the presence of a regional high- to medium-temperature event under low-pressure conditions (< 6 kbar) to explain Mesozoic monazite ages. Since monazite (re)growth resulting from fluid-assisted metasomatic processes is well-documented (e.g., Budzyń et al. 2011; Harlov et al. 2011; Williams et al. 2011), Mesozoic monazite ages may thus constrain the timing of metasomatism recorded by fluid inclusions, further supported by the stability of monazite in the presence of NaCl brines (Budzyń et al. 2011). In addition, well-documented dissolution-reprecipitation microstructures in monazites of the

454 study area (Oriolo et al. 2019) could be explained by circulation of high-Ca-bearing brines,
455 which promote monazite dissolution (Budzyń et al. 2011).

456 As further supported by regional evidence (e.g., Páez et al. 2010; Castro et al.
457 2011a, 2011b; Martínez Dopico et al. 2017; Suárez and González 2018), fluid flow and
458 metasomatism recorded by fluid inclusions were thus likely related to a Jurassic
459 tectonomagmatic event. However, they might also have been linked, at least partially, to
460 Cretaceous and/or Cenozoic hydrothermal processes, which were reported for the study
461 area as well (Giacosa et al. 2001). Though Cenozoic magmatism is well-documented by
462 geochronological data and field relationships (e.g., Rapela et al. 1988; Bechis et al. 2014),
463 the existence of Cretaceous magmatism is uncertain due to the lack of high-precision
464 geochronological data. However, Cretaceous volcanism is exposed immediately northwest
465 (Aragón et al. 2011) and significant Cretaceous exhumation associated with an early
466 Andean tectonothermal event has been regionally recognized in the North Patagonian
467 Andes (Orts et al. 2012; Oriolo et al. 2019; Olaizola et al. 2020).

468 Basement fabrics played a major role as first-order structural controls in the
469 evolution of Mesozoic and Cenozoic magmatic and sedimentary processes in northern
470 Patagonia (Renda et al. 2019). In the particular case of the study area, microstructural
471 evidence of basement rocks suggests significant reactivation of metamorphic fabrics and
472 deformation-assisted replacement reactions during retrograde metamorphism (Oriolo et al.
473 2019). The Paleozoic metamorphic foliation might thus represent an effective pathway
474 allowing fluid circulation, which in turn promoted retrograde metamorphic reactions and
475 reequilibration in an otherwise dry and thus less reactive crustal section (e.g., Jamtveit et al.
476 2000; Altree-Williams et al. 2015). In this context, the possible reactivation of
477 metamorphic fabrics (Oriolo et al. 2019) might be crucial for generating secondary porosity

478 due to generation of open spaces, where fluids could circulate and further increase porosity
479 by hydraulic fracturing and dissolution-reprecipitation, as supported by healed
480 microfractures and compositional changes revealed by CL data.
481
482 **Conclusions**

483 Clino-amphibole experimentally formed after heating in ferropyrosmalite-bearing
484 fluid inclusions, suggesting that ferropyrosmalite was formed as a retrograde phase in fluid
485 inclusions in the studied quartz crystals. The reaction implies the uptake of Fe^{2+} and Cl^-,
486 and the enrichment of Ca^{2+} in the brine. These Cl-rich high salinity brines promoted
487 metasomatism, fluid-assisted deformation and dissolution-reprecipitation processes, as
488 documented by channelway microstructures, healed microfractures and compositional
489 changes in quartz revealed by the cathodoluminescence microscopy. Basement fabrics
490 probably represented effective pathways for fluid flow, which promoted retrograde mineral
491 reactions.

492 Ferropyrosmalite-bearing inclusions represent the fluids originated from post-peak
493 metamorphic Mesozoic magmatism, most likely of Jurassic age, represented by widespread
494 granitoids intruding the basement. However, Cretaceous and Cenozoic tectonomagmatic
495 processes cannot be ruled out as triggers of hydrothermal processes, at least to some extent.
496 All these fluids were associated with regional metasomatism related to retrograde high- to
497 medium-temperature and low-pressure tectonothermal events, which largely overprinted
498 the metamorphic basement of the northern Patagonia.
499
500 **Acknowledgements**

Sebastián Oriolo acknowledges financial support of the National Geographic Society (grant CP-123R17) and Agencia Nacional de Promoción Científica y Tecnológica (PICT-2017-1092). The reviews and constructive comments made by Peter Koděra (Comenius University Bratislava, Slovak Republic) and David Jenkins (Binghamton University, New York, USA) are highly acknowledged. The authors also thank Burkhard Schmidt for his assistance during Raman analysis.

References

Altree-Williams, A., Pring, A., Ngothai, Y., and Brugger, J. (2015) Textural and compositional complexities resulting from coupled dissolution-reprecipitation reactions in geomaterials. Earth-Science Reviews, 150, 628-651.

Apopei, A.I., and Buzgar, N. (2010) The Raman study of amphiboles. Analele Ştiinţifice de Universităţii Al. I. Cuza Iaşi Geologie, 56, 57-83.

Aragón, E., Castro, A., Díaz-Alvarado, J., and Liu, D.-Y. (2011) The North Patagonian batholith at Paso Puyehue (Argentina-Chile). SHRIMP ages and compositional features. Journal of South American Earth Sciences, 32, 547-554.

Assarsson, G.O. (1950) The quaternary system $CaCl_2$-KCl-NaCl-H_20. Journal of the American Chemical Society, 72, 1433-1436.

Bakker, R.J. (2017) Re-equilibration processes in fluid inclusion assemblages. Minerals, 7, 117.

Banaszak, M. (2014) Differentiation regimes in the Central Andean magma systems: case studies of Taapaca and Parinacota volcanoes, Northern Chile, 238 p. Ph.D. thesis, University of Göttingen, Göttingen.

Bechis, F., Encinas, A., Concheyro, A., Litvak, V.D., Aguirre-Urreta, B., and Ramos, V.A. (2014) New age constraints for the Cenozoic marine transgressions of northwestern Patagonia, Argentina (41°-43° S): Paleogeographic and tectonic implications. Journal of South American Earth Sciences, 52, 72-93.

Behr, H.-J., and Frentzel-Beyme, K. (1987) Permeability and paleoporosity in crystalline bedrocks of the Central European Basement – Studies of cathodoluminescence. In H.J. Behr and C.B. Raleigh, C.B., Eds., Exploration of the deep continental crust, 2, p. 477-497. Springer, Berlin Heidelberg New York.

Bodnar, R.J. (2003) Introduction to aqueous electrolyte fluid inclusions. In I. Samson, A. Anderson, D. Marshall, Eds., Fluid inclusions: Analysis and interpretation, 32, p. 81-100. Mineralogical Association of Canada, Vancouver.

Borrok, D.M., Kelser, S.E., Boer, R.H., and Essene, E.J. (1998) The Vergenoeg magnetite-fluorite deposit, South Africa: Support for a hydrothermal model for massive iron oxide deposits. Economic Geology, 93, 564-586.

Budzyń, B., Harlov, D.E., Williams, M.L., and Jercinovic, M.J. (2011) Experimental determination of stability relations between monazite, fluorapatite, allanite, and REE-epidote as a function of pressure, temperature, and fluid composition. American Mineralogist, 96, 1547-1567.

Burke, E.A.J. (2001) Raman microspectrometry of fluid inclusions. Lithos, 55, 139-158.

Castro, A., Moreno-Ventas, I., Fernández, C., Vujovich, G., Gallastegui, G., Heredia, N., Martino, R.D., Becchio, R., Corretgé, L.G., Díaz-Alvarado, J., Such, P., García-Arias, M., and Liu, D.-Y. (2011a) Petrology and SHRIMP U-Pb zircon geochronology of Cordilleran granitoids of the Bariloche area, Argentina. Journal of South American Earth Sciences, 32, 508-530.

Castro, A., Aragón, E., Díaz-Alvarado, J., Blanco, I., García-Casco, A., Vogt, K., and Liu, D.-Y. (2011b) Age and composition of granulite xenoliths from Paso de Indios, Chubut province, Argentina. Journal of South American Earth Sciences, 32, 567-574.

Cepedal, A., Fuertes-Fuente, M., Martín-Izard, A., and Boiron, M.-C. (2003). Fluid composition in Ortosa Au-skarn and El Valle-Boinás Cu-Au skarn, Río Narcea Gold Belt (Spain). Acta Mineralogica-Petrographica, 2, 36-37.

Dalla Salda, L.H., Cingolani, C.A., and Varela, R. (1991) El basamento cristalino de la región norpatagónica de los lagos Gutiérrez, Mascardi y Guillelmo, provincia de Río Negro. Revista de la Asociación Geológica Argentina, 46, 263-276.

Dong, G., and Pollard, P.J. (1997) Identification of ferropyrosmalite by Laser Raman microprobe in fluid inclusions from metalliferous deposits in the Cloncurry District, NW Queensland, Australia. Mineralogical Magazine, 61, 291-293.

Fall, A., Tattitch, B., Bodnar, R.J. (2011) Combined microthermometric and Raman spectroscopic technique to determine the salinity of H2O-CO2-NaCl fluid inclusions based on clathrate melting. Geochimica et Cosmochimica Acta, 75, 951-964.

Fornero, E., Allegrina, M., Rinaudo, C., Mazziotti-Tagliani, S., Gianfagna, A. (2008). Micro-Raman spectroscopy applied on oriented crystals of fluoro-edenite amphibole. Periodico di Mineralogia, 77, 5-14.

Frezzotti, M.L., Tecce, F., and Casagli, A. (2012) Raman spectroscopy for fluid inclusion analysis. Journal of Geochemical Exploration, 112, 1-20.

García-Sansegundo, J., Farías, P., Gallastegui, G., Giacosa, R.E., and Heredia, N. (2009) Structure and metamorphism of the Gondwanan basement in the Bariloche region (North Patagonian Argentine Andes). International Journal of Earth Sciences, 98, 1599-1608.

Giacosa, R., Heredia, N., Césari, O., and Zubia, M. (2001) Hoja 4172-IV, San Carlos de Bariloche (provincias de Río Negro y Bariloche), 77 p. Instituto de Geología y Recursos Minerales (IGRM) – SEGEMAR, Buenos Aires.

Giesting, P.A., Filiberto, J. (2016). The formation environment of potassic-chloro-hastingsite in the nakhlites MIL 03346 and pairs and NWA 5790: Insights from terrestrial chloro-amphibole. Meteoritics & Planetary Science, 51, 2127-2153.

González Díaz, E.F. (1982) Chronological zonation of granitic plutonism in the Northern Patagonian Andes of Argentina: the migration of intrusive cycles. Earth-Science Reviews, 18, 365-393.

Hanley, J.J., and Mungall, J.E. (2003) Chlorine enrichment and hydrous alteration of the Sudbury breccia hosting footwall Cu-Ni-PGE mineralization at the Fraser mine, Sudbury, Ontario, Canada. The Canadian Mineralogist, 41, 857-881.

Harlov, D., and Austrheim, H. (2012) Metasomatism and the chemical transformation of rock: The role of fluids in terrestrial and extraterrestrial processes, 806 p. Springer, Berlin Heidelberg.

Harlov, D.E., Wirth, R., and Hetherington, C.J. (2011) Fluid-mediated partial alteration of monazite: The role of coupled dissolution-reprecipitation during apparent solid state element mass transfer. Contributions to Mineralogy and Petrology, 162, 329-348.

Jamtveit, B., Austrheim, H., and Malthe-Sørenssen, A. (2000) Accelerated hydration of the Earth's deep crust induced by stress perturbations. Nature, 408, 75-78.

Jenkins, D.M. (2019). The incorporation of chlorine into calcium amphibole. American Mineralogist, 104, 514-524.

Koděra, P., Rankin, A.H., and Lexa, J. (1998) Evolution of fluids responsible for iron skarn mineralisation: An example from the Vyhne-Klokoč deposit, Western Carpathians, Slovakia. Mineralogy and Petrology, 64, 119-147.

Koděra, P., Murphy, P.J., and Rankin, A.H. (2003) Retrograde mineral reactions in saline fluid inclusions: The transformation ferropyrosmalite ↔ clinopyroxene. American Mineralogist, 88, 151-158.

Kwak, T.A.P. (1986) Fluid inclusions in skarns (carbonate replacement deposits). Journal of Metamorphic Geology, 4, 363-384.

Lafuente B., Downs R. T., Yang H., and Stone N. (2015) The power of databases: the RRUFF project. In: Highlights in Mineralogical Crystallography, T. Armbruster and R. M. Danisi, eds. Berlin, Germany, W. De Gruyter, pp 1-30

Leissner L., Schlüter, J., Horn, I., and Mihailova B. (2015) Exploring the potential of Raman spectroscopy for crystallochemical analyses of complex hydrous silicates: I. Amphiboles. American Mineralogist, 100, 2682–2694.

Li, C., and Naldrett, A.J. (1993) High chlorine alteration minerals and calcium-rich brines in fluid inclusions from the Strathcona deep copper zone, Sudbury, Ontario. Economic Geology, 88, 1780-1796.

Martínez, J.C., Dristas, J.A., and Massonne, H.-J. (2012) Palaeozoic accretion of the microcontinent Chilenia, North Patagonian Andes: high-pressure metamorphism and subsequent thermal relaxation. International Geology Review, 54, 472-490.

Martínez Dopico, C.I., Tohver, E., López de Luchi, M.G., Wemmer, K., Rapalini, A.E., and Cawood, P.A. (2017). Jurassic cooling ages in Paleozoic to early Mesozoic granitoids of northeastern Patagonia: $^{40}Ar/^{39}Ar$, ^{40}K-^{40}Ar mica and U-Pb zircon evidence. International Journal of Earth Sciences, 106, 2343-2357.

Matthews, A.N. (1976) Magnetite formation by the reduction of hematite with iron under hydrothermal conditions. American Mineralogist, 61, 927-932.

Neuser, R.D., Bruhn, F., Götze, J., Habermann, D. and Richter, D.K. (1995) Cathodoluminescence: method and application. Zentralblatt für Geologie und Paläontologie, 1-2, 287-306.

Oakes, C.S., Bodnar, R.J., and Simonson, J.M. (1990) The system NaCl-CaCl2-H2O: I. The ice liquidus at 1 atm total pressure. Geochimica et Cosmochimica Acta, 54, 603-610.

Olaizola, E.R., Bechis, F., Ballesteros, J., Oriolo, S., Christie Newbery, J., and Yagupsky, D.L. (2020) Análisis de la evolución cinemática y exhumación asociadas a las fases de deformación registradas en los Andes Norpatagónicos a los 41°50´ S. XXI Congreso Geológico Argentino, Puerto Madryn.

Oriolo, S., Schulz, B., González, P. D., Bechis, F., Olaizola, E., Krause, J., Renda, E., and Vizán, H. (2019) The Late Paleozoic tectonometamorphic evolution of Patagonia revisited: Insights from the pressure-temperature-deformation-time (P-T-D-t) path of the Gondwanide basement of the North Patagonian Cordillera (Argentina). Tectonics, 38, 2378-2400. https://doi.org/10.1029/2018TC005358

Orts, D.L., Folguera, A., Encinas, A., Ramos, M., Tobal, J., and Ramos, V.A. (2012) Tectonic development of the North Patagonian Andes and their related Miocene foreland basin (41° 30′-43° S). Tectonics, 31, TC3012.

Páez, G.N., Ruiz, R., Guido, D.M., Jovic, S.M., and Schalamuk, I.B. (2010) The effects of K-metasomatism in the Bahía Laura Volcanic Complex, Deseado Massif, Argentina: Petrologic and metallogenic consequences. Chemical Geology, 273, 300-313.

Pan, Y., Fleet, M.E., Barnett, R.L., and Chen, Y. (1993) Pyrosmalite in Canadian Precambrian sulfide deposits; mineral chemistry, petrogenesis and significance. The Canadian Mineralogist, 31, 695-710.

Putnis, A. (2009) Mineral replacement reactions. Reviews in Mineralogy and Geochemistry, 70, 87-124.

Putnis, A., and Austrheim, H. (2010) Fluid-induced processes: metasomatism and metamorphism. Geofluids, 10, 254-269.

Putnis, A., and John, T. (2010) Replacement processes in the Earth's crust. Elements, 6, 159-164.

Raič, S., Mogessie, A., Krenn, K., Hauzenberger, C.A., and Tropper, P. (2018) Deciphering Magmatic and Metasomatic Processes Recorded by Fluid Inclusions and Apatite within the Cu-Ni±PGE-Sulfide Mineralized Bathtub Intrusion of the Duluth Complex, NE Minnesota, USA. Journal of Petrology, 59, 1167-1192.

Rapela, C.W., Spalletti, L.A., Merodio, J.C., and Aragón, E. (1988) Temporal evolution and spatial variation of early Tertiary volcanism in the Patagonian Andes (40°S - 42°30'S). Journal of South American Earth Sciences, 1, 75-88.

Rebay, G., Riccardi, M.P., Spalla, M.I. (2015) Fluid rock interactions as recorded by Cl-rich amphiboles from continental and oceanic crust of Italian orogenic belts. Periodico di Mineralogia, 84, 751-777.

Renda, E.M., Alvarez, D., Prezzi, C., Oriolo, S., and Vizán, H. (2019) Inherited basement structures and their influence in foreland evolution: A case study in Central Patagonia, Argentina. Tectonophysics, 772, 228232.

Roedder, E. (1962) Ancient fluids in crystals. Scientific American, 207, 38-47.

Rösche, C. (2018) Thermal stability and oxidation processes in amphiboles on the tremolite-ferro-actinolite join studied by Raman spectroscopy. BSc. Thesis, University of Hamburg.

Ruiz-Agudo, E., Putnis, C.V., and Putnis, A. (2014) Coupled dissolution and precipitation at mineral-fluid interfaces. Chemical Geology, 383, 132-146.

Steele-MacInnis, M., Bodnar, R.J. and Naden, J. (2011) Numerical model to determine the composition of H_2O-NaCl-$CaCl_2$ fluid inclusions based on microthermometric and microanalytical data. Geochimica et Cosmochimica Acta, 75, 21-40.

Suárez, R.J., and González, P.D. (2018) Caracterización geológica del metamorfismo diastatermal mesozoico en la Cuenca Neuquina y su relación con la anomalía térmica en el sinrift. Revista de la Asociación Geológica Argentina, 75, 457-472.

Tazava, E., Oliveira, C.G., and Souza Gomes, N. (1999) Ocorrência de ferropirosmalita nas brechas mineralizadas do depósito de Au-Cu-(±ETR-U) de Igarapé Bahia, província mineral de Carajás. Revista Brasileira de Geociências, 29, 345-348.

Touret, J.L.R. (2001) Fluids in metamorphic rocks. Lithos, 55, 1-25.

Van den Kerkhof, A.M., and Hein, U.F. (2001) Fluid inclusion petrography. Lithos, 55, 27-47.

679 Van den Kerkhof, A.M., Riganti, A., Scherer, T., Kronz, A., and Simon K. (2004) Origin
680 and evolution of Archean quartzites from the Nondweni greenstone belt (South Africa):
681 inferences from a multidisciplinary study. South African Journal of Geology, 107, 559-576.

682 Van den Kerkhof, A., Kronz, A., and Simon, K. (2014) Deciphering fluid inclusions in
683 high-grade rocks. Geoscience Frontiers, 5, 683-695.

684 Vaughan, J.P. (1986) The iron end-member of the pyrosmalite series from the Pegmont
685 lead-zinc deposit, Queensland. Mineralogical Magazine, 50, 527-531.

686 Vityk, M.O., and Bodnar, R.J. (1995) Do fluid inclusions in high-grade metamorphic
687 terranes preserve peak metamorphic density during retrograde decompression? American
688 Mineralogist, 80, 641-644.

689 Volfinger, M., Robert, J.-L., Vielzeuf, D., Neiva, A.M.R. (1985) Structural control of the
690 chlorine content of OH-bearing silicates (micas and amphiboles). Geochimica et
691 Cosmochimica Acta, 49, 37-48.

692 Wagner, T., Fusswinkel, T., Wälle, M., and Heinrich, C.A. (2016) Microanalysis of fluid
693 inclusions in crustal hydrothermal systems using laser ablation methods. Elements, 12, 323-
694 328.

695 Wanhainen C., Broman C., Martinsson O., and Magnor B. (2012) Modification of a
696 Palaeoproterozoic porphyry-like system: Integration of structural, geochemical,
697 petrographic, and fluid inclusion data from the Aitik Cu–Au–Ag deposit, northern Sweden.
698 Ore Geology Reviews, 48, 306-331.

699 Williams, M.L., Jercinovic, M.J., Harlov, D.E., Budzyń, B., and Hetherington, C.J. (2011)
700 Resetting monazite ages during fluid-related alteration. Chemical Geology, 283, 218-225.

701 Yang, H., Downs, R.T., Yang, Y.W., and Allen, W.H. (2012) Pyrosmalite-(Fe),
702 $Fe_8Si_6O_{15}(OH, Cl)_{10}$. Acta Crystallographica Section E: Structure Reports Online, 68, i7-i8.

703 Yardley, B.W.D., and Bodnar, R.J. (2014) Fluids in the continental crust. Geochemical
704 Perspectives, 3, 1-127.

705 Zharikov, V.A., Pertsev, N.N., Rusinov, V.L., Callegari, E., and Fettes, D.J. (2007)
706 Metasomatism and metasomatic rocks, 17 p. Recommendations by the IUGS
707 Subcommission on the Systematics of Metamorphic Rocks, International Union of
708 Geological Sciences (IUGS).

709 Zwart E.W., and Touret J.L.R. (1994) Melting behaviour and composition of aqueous fluid
710 inclusions in fluorite and calcite: applications within the system H_2O-$CaCl_2$-NaCl.
711 European Journal of Mineralogy, 6, 773-786.

712

713 **Figure captions**

714

Fig. 1. Geological map of the study area (modified after González Bonorino 1973; García-Sansegundo et al. 2009; Bechis et al. 2014; Oriolo et al. 2019). EPMA Th-U-Pb monazite geochronological data (1: Martínez et al. 2012; 2: Oriolo et al. 2019) are shown.

Fig. 2. a) Quartz segregations parallel to S_2 metamorphic foliation of paragneisses. b) F_2 tight folds showing rootless hinges defined by quartz segregations (arrows). c) Retrograde chlorite, white mica and opaque minerals showing shape-preferred orientation parallel to subhorizontal S_2 planes (cross-polarized light). d) Randomly oriented aggregates of chlorite, actinolite and white mica cross-cutting subhorizontal S_2 planes (cross-polarized light). Act: actinolite, Chl: chlorite, Op: opaque minerals, Wmca: white mica.

Fig. 3. Microphotographs of quartz segregation thin sections in cathodoluminescence (left) and transmitted light (crossed polarizers, right). CL microstructures are indicative of high-temperature (a, b; sample BA 28-18, López hill) and low-temperature alteration (c, sample BA 6-18, Jakob lake). 1 = secondary zoning; 2 = grain boundary alteration; 3 = channelway microstructure showing initial blue CL; 4 = polymineralic channelway showing brown CL; 5 = healed cataclastic microstructures observed for initial (blue) and final (violet and reddish) CL; 6 = subgrains.

Fig. 4. Microphotographs showing multiphase fluid inclusions from the Lopez hill location. a) Natural, non-heated inclusion containing halite and a hexagonal crystal of ferropyrosmalite; b) Natural, non-heated inclusion containing halite, sylvite, hematite, and ferropyrosmalite; c) Same inclusions as (b) after heating over 570 °C. Dissolution of ferropyrosmalite and hematite favours crystallization of clino-amphibole and magnetite, respectively. Note that, after the reaction, two prismatic amphibole crystals formed in the same inclusion. The Raman spectrum of amphibole is shown in Figure 7b (polarized spectra, recording OH^- stretching bands); d) Natural, non-heated inclusion containing halite, magnetite and ferropyrosmalite; e) Same inclusion as (d) after heating. The resulting clino-amphibole, identified as chloro-hastingsite, lacks in OH^- peaks, suggesting substitution of OH^- by Cl^- (Fig. 7b, unpolarized spectrum). Hl: halite, Fp: ferropyrosmalite, V: vapor, L: liquid, Syl: sylvite, Hem: hematite, Amp: amphibole, Mag: magnetite.

Fig. 5. Microthermometric results of fluid inclusions. a) Liquid-vapor homogenization temperatures (V: vapor, L: liquid) for early secondary multiphase and late secondary biphasic inclusions; b) Melting temperatures of daughter crystals in the early secondary multiphase inclusions (halite and ferropyrosmalite); c) Brine salinity and total salinity of early secondary multiphase inclusions and late secondary (L-V and V-L) inclusions.

Fig. 6. Fluid inclusion compositions in the system H_2O-NaCl-$CaCl_2$ (modified after Oakes et al. 1990; Zwart and Touret 1994). AA: antarcticite, Hl: halite, HH: hydrohalite. Red squares: early secondary multiphase inclusions (total salinity), red circles: early secondary L+V±S multiphase inclusions (brine salinity without halite crystals), blue area: late secondary V-L and L-V inclusions.

Fig. 7. Raman spectra of daughter phases in (a) natural, non-heated inclusions showing spectra for ferropyrosmalite and hematite (inclusion in Fig. 4b), and (b) heated inclusions

755 showing spectra for clino-amphibole with OH^- vibration bands in polarized laser light with
756 orientations parallel and perpendicular to the crystallographic c-axis (inclusion in Fig. 4c)
757 and Cl-bearing clino-amphibole (unpolarized laser light; inclusion in Fig. 4e). Raman peaks
758 for the host quartz are subtracted and not shown here.

759

760 **Table 1.** Overview of fluid inclusion data obtained from microthermometry with indication
761 of the relative abundance and number of measured fluid inclusions (n). The phase volume
762 fractions at room temperature are estimated for the liquid (L), solid (S) and vapor (V)
763 phases. Phase transition temperatures are given for the melting of CO_2 (T_m CO_2), the
764 eutectic temperature (T_e), ice melting (T_m ice), hydrohalite (T_m HH), clathrate melting (Tm
765 clathrate), liquid-vapor homogenization (T_h L-V) into the liquid (L) or vapor phase (V),
766 sylvite dissolution (T_m Syl), halite dissolution (T_m HI), and ferropyrosmalite dissolution
767 (T_m Fp). Salinities were calculated from the microthermometry data and the models of
768 Steele-McInnes et al. (2011) and Oakes et al. (1990). Mean values are given in brackets.

		Early secondary inclusions		Late secondary inclusions	
		H_2O-NaCl-$CaCl_2$ ± Solids ± CO_2		**H_2O-NaCl ± CO_2 ± N_2 ± H_2S**	
		Multiphase	**L+V (±S)**	**L+V (±S)**	**V+L (±S)**
		Abundant (n=39)	*Rare (n=3)*	*Abundant (n=33)*	*Abundant (n=17)*
Phase volume fractions	**L**	0.10 - 0.65 (0.31)	0.30 - 0.40	0.70 - 0.87 (0.81)	0.05 - 0.30 (0.14)
	S	0.05 - 0.70 (0.53)	0 - 0.40	0 - 0.05	0 - 0.05
	V	0 - 0.65 (0.16)	0.20 - 0.70	0.10 - 0.30 (0.19)	0.75 - 0.95 (0.87)
Phase transition temperatures (°C)	**T_m CO_2**	-57.5 - -56.9	n.o.	n.o.	n.o.
	T_e	-56 - -54	ca. -58	-21.4 - -21.0	n.o.
	T_m ice	-46.3 - -28.1 (-36.6)	ca. -32	-3.2 - 1.5 (-0.7)	-3.2 - 0
	T_m HH	-20.4 - -12.0 (-16.5)	-15.9 - -15.0	-	-
	T_m clathrates	n.o.	(0.2)	n.o.	n.o.
	T_h L-V	256 - 515 L (381)	251 L - >350 V	254 - 384 L (296)	319 - 389 V (361)
	T_m Syl	ca. 190	-	-	-
	T_m HI	287 - 556 (489)	-	-	-
	T_m Fp	550 - 581 (560)	-	-	-
Calculated salinity (wt. %)	**Total salinity**	27 - 73	27 - 30	0 - 5	0 - 5
	NaCl ± KCl	4 - 64	8 - 11	0 - 5	0 - 5
	$CaCl_2$	10 - 26	15 - 20	-	-

71°25' W

41°09' S

41°20' S

N

Nahuel Huapi lake

López hill

169.6 ± 6.7 Ma (1)

Negra lake

Jakob lake

Catedral hill

170 ± 7 Ma (2)
110 ± 10 Ma (2)

Gutiérrez lake

Ñireco hill

302 ± 16 Ma (2)
299 ± 8 Ma (2)
171 ± 9 Ma (2)
80 ± 20 Ma (2)

Challhuaco hill

391.7 ± 4.0 Ma (1)
350.4 ± 5.8 Ma (1)

Brazo Tronador

Mascardi lake

Quaternary deposits

Olig.-Mio. volcano-sedimentary rocks

Mesozoic and Cenozoic intrusions

Igneous-metamorphic basement

Sample location

5 km

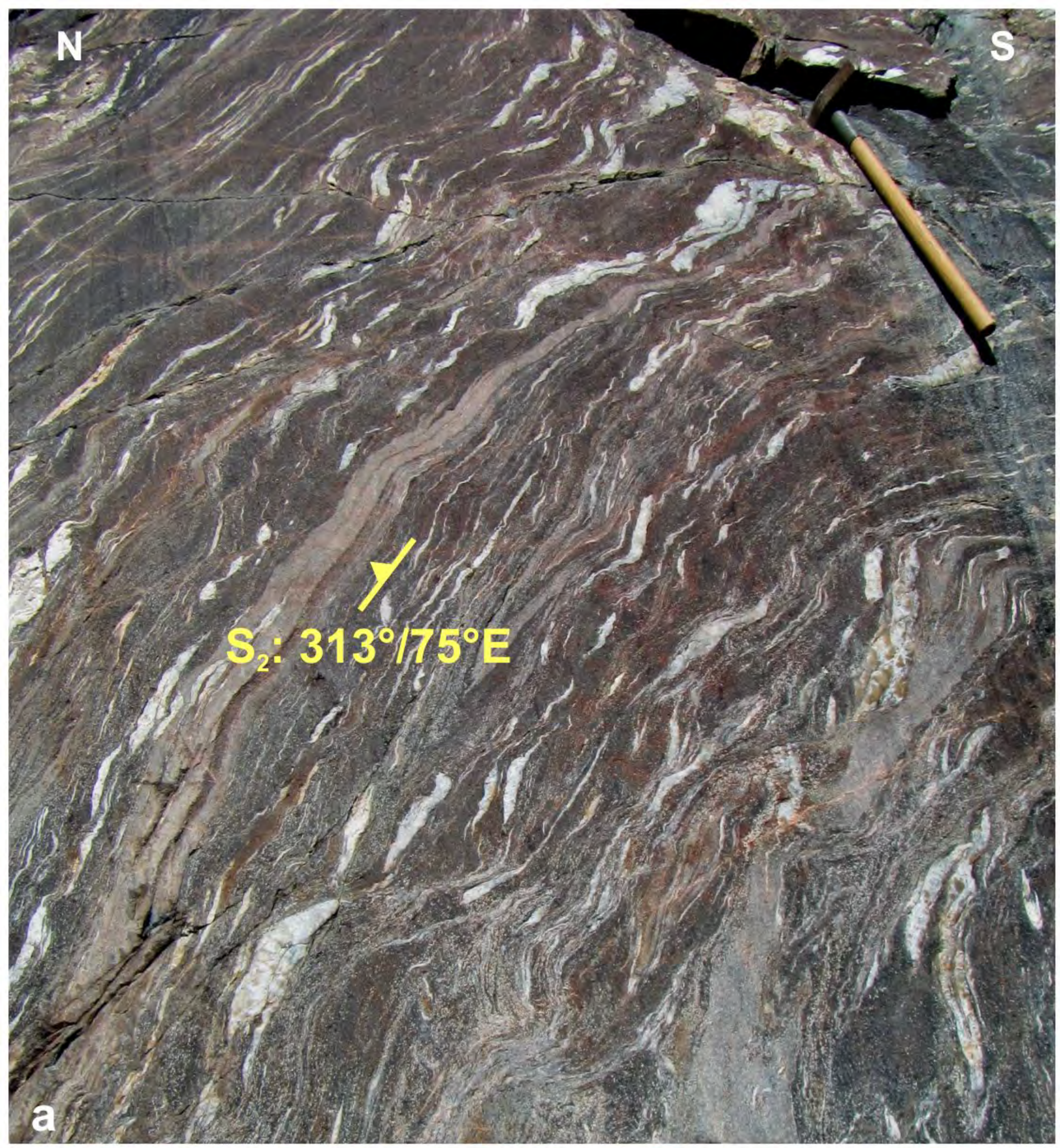
N
S
S_2: 313°/75°E
a


WNW
SSE
F_2
b

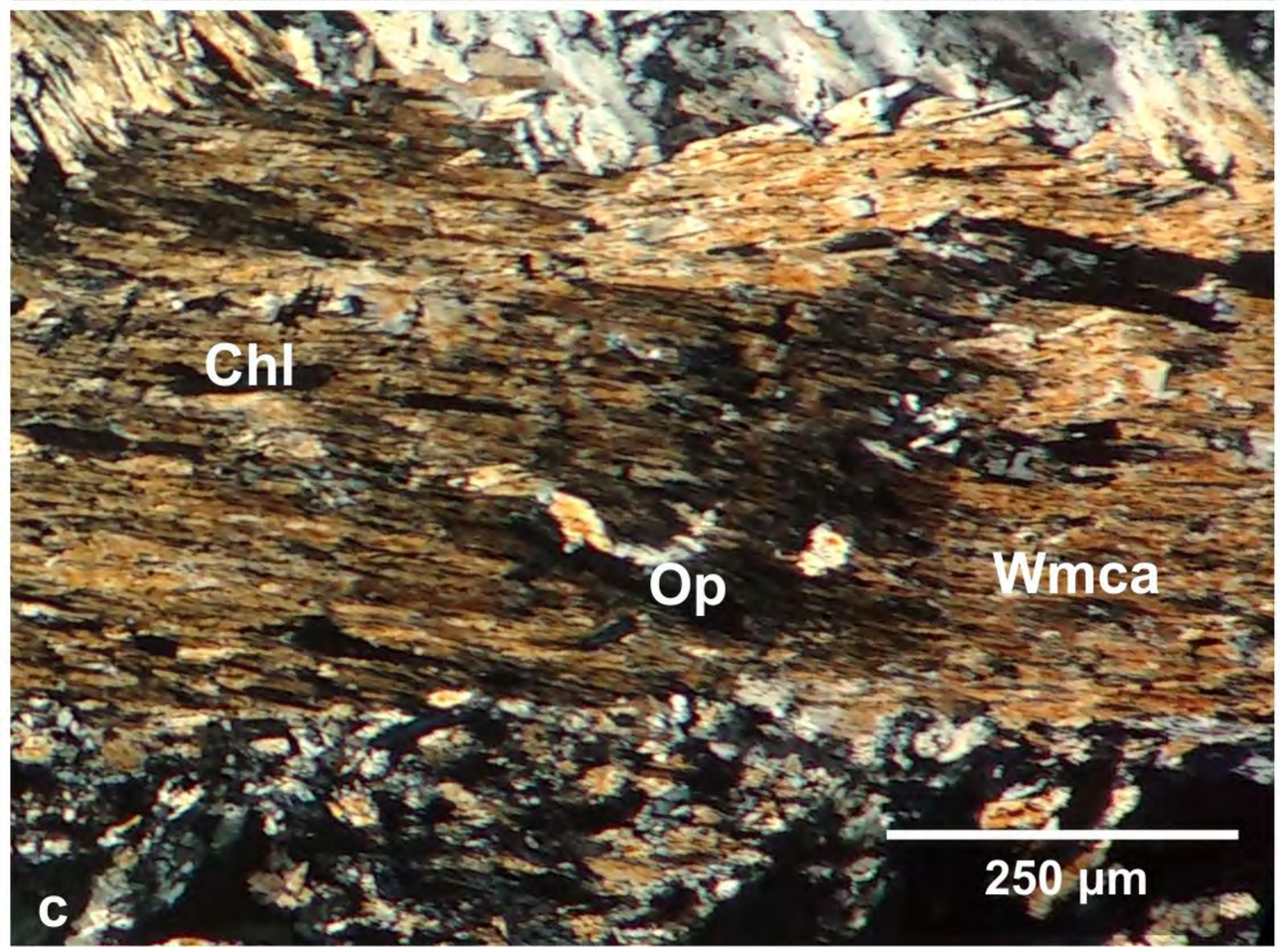
Chl
Op
Wmca
250 µm
c

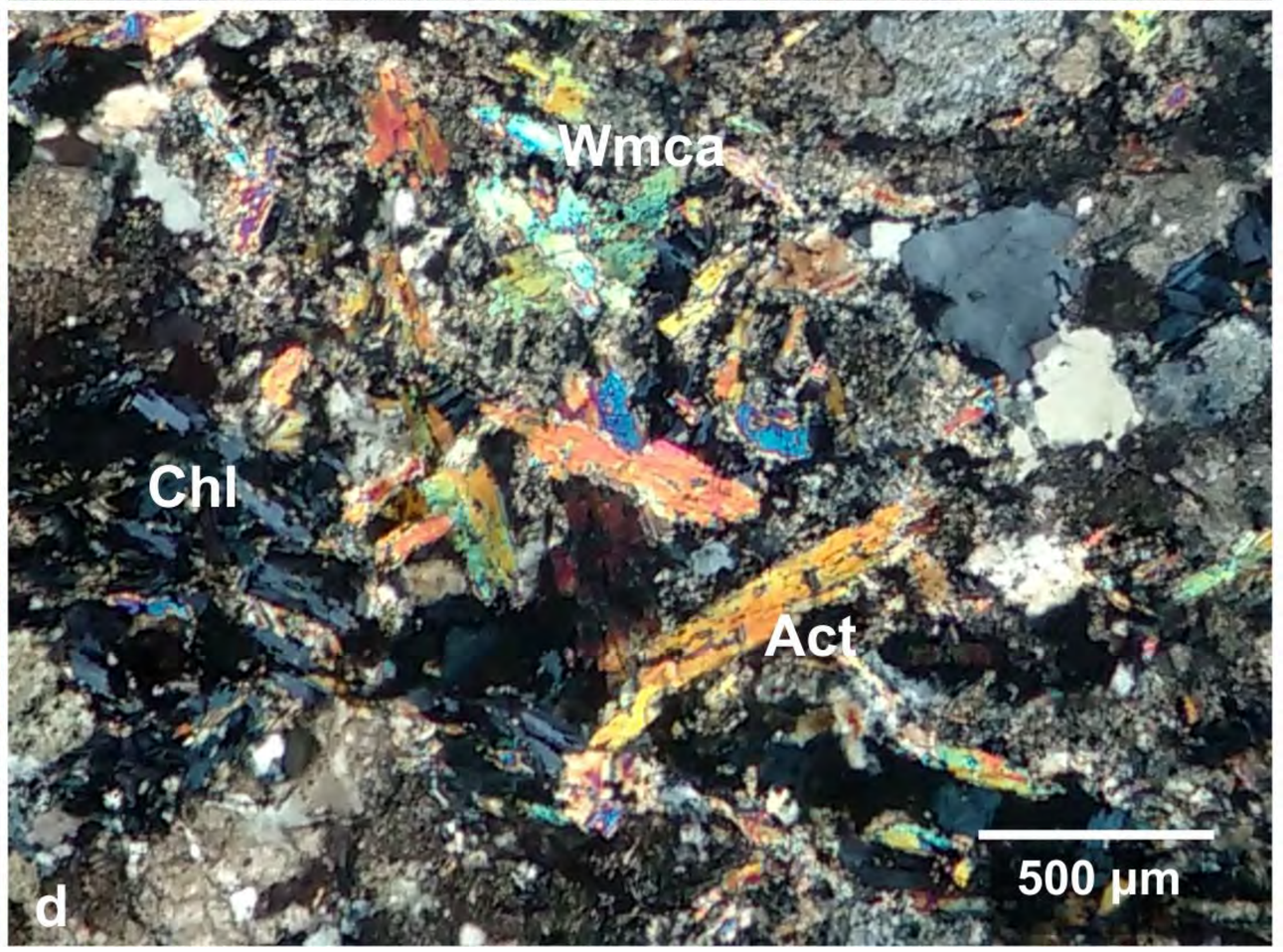
Wmca
Chl
Act
500 µm
d

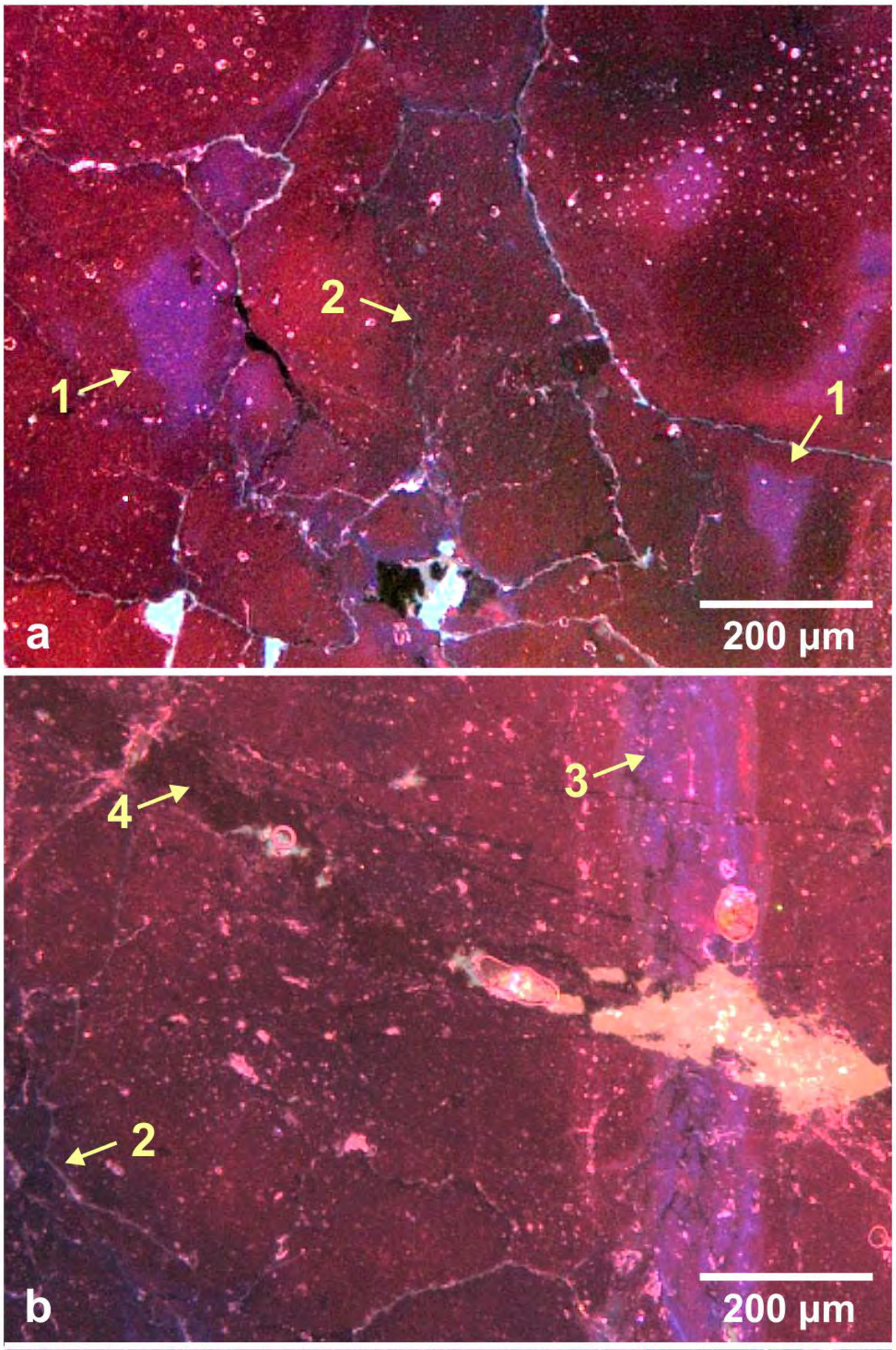
1
2
1
a
200 µm

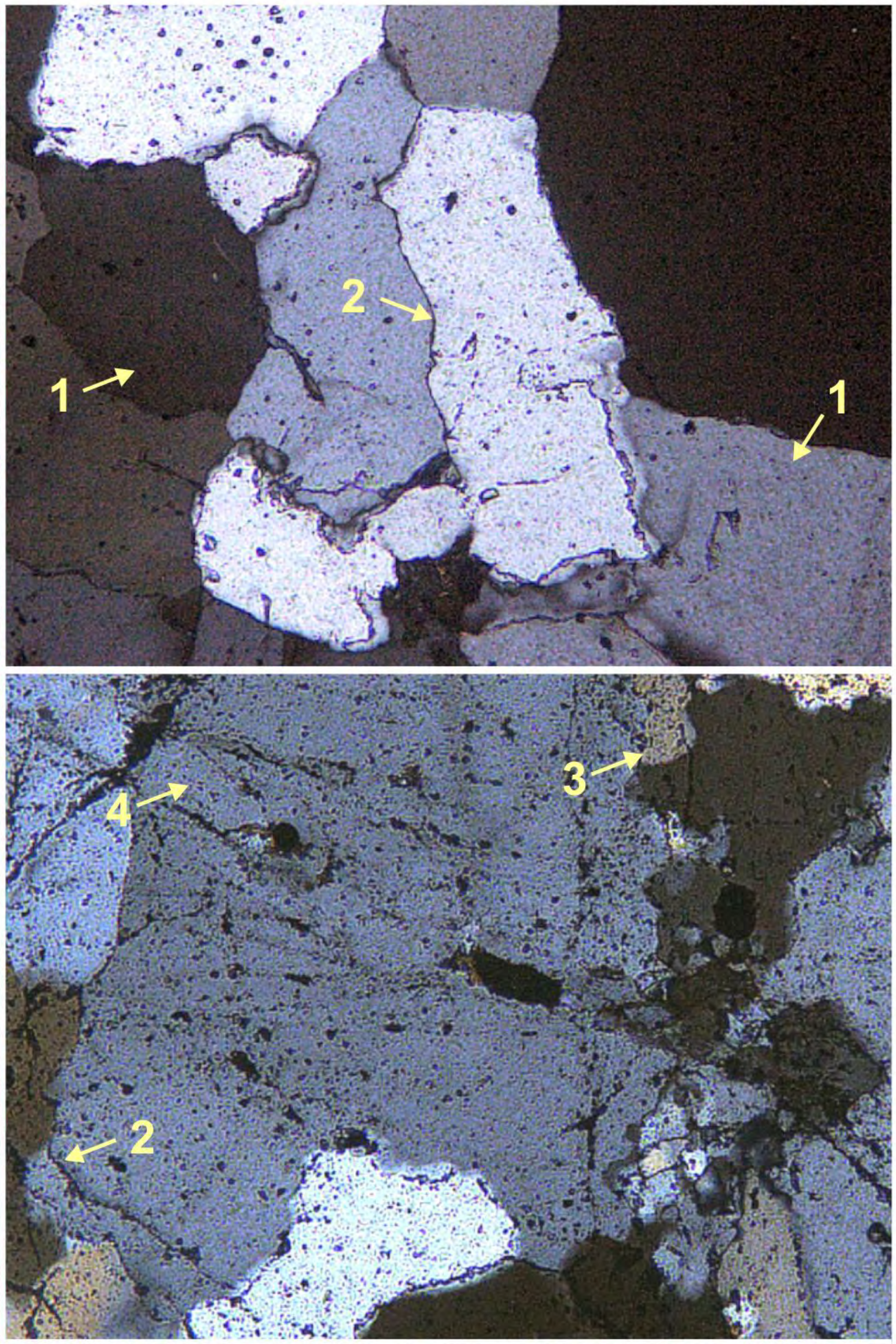
1
2
1

4
3
2
b
200 µm

4
3
2

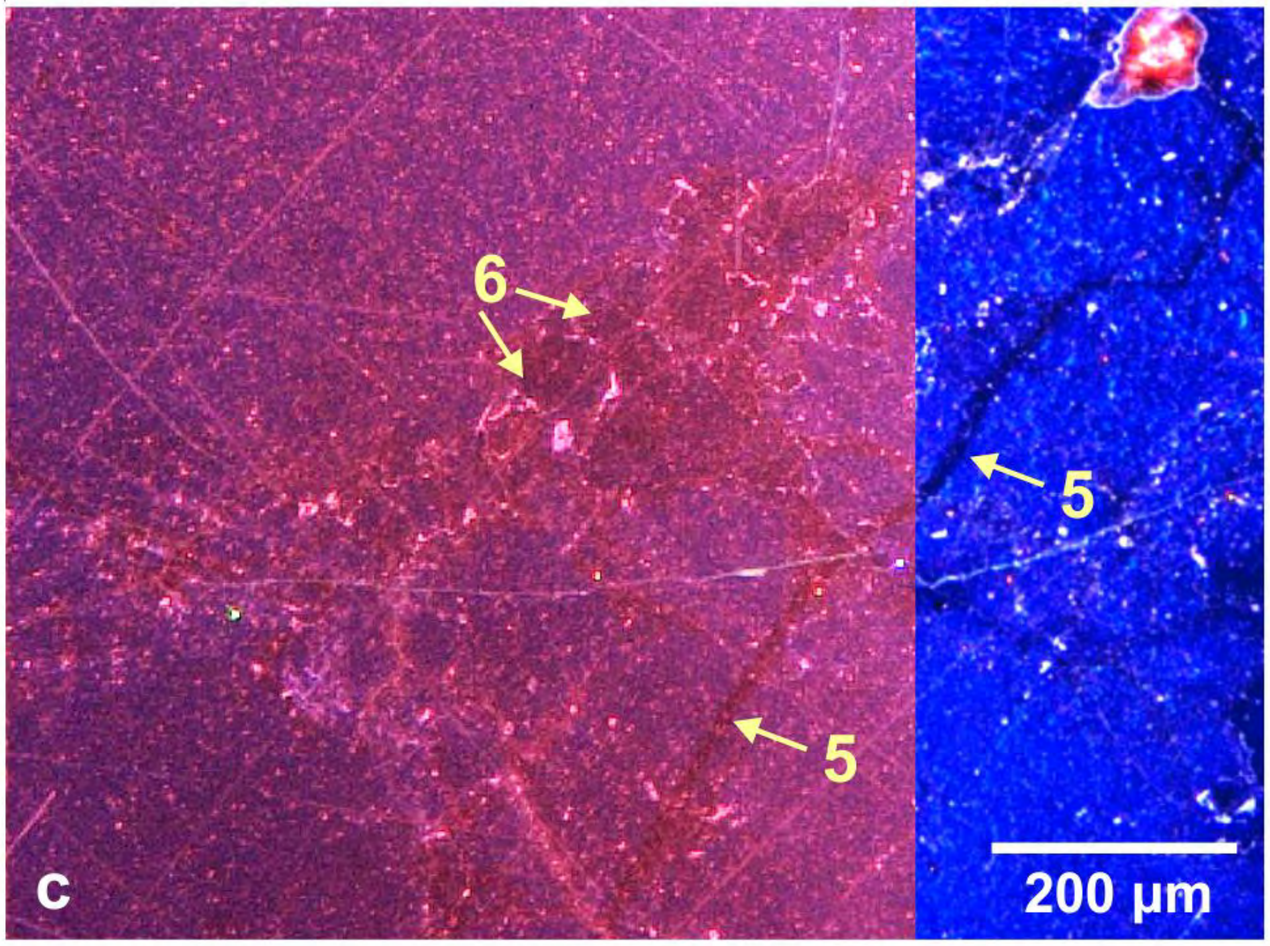
6
5
c
200 µm

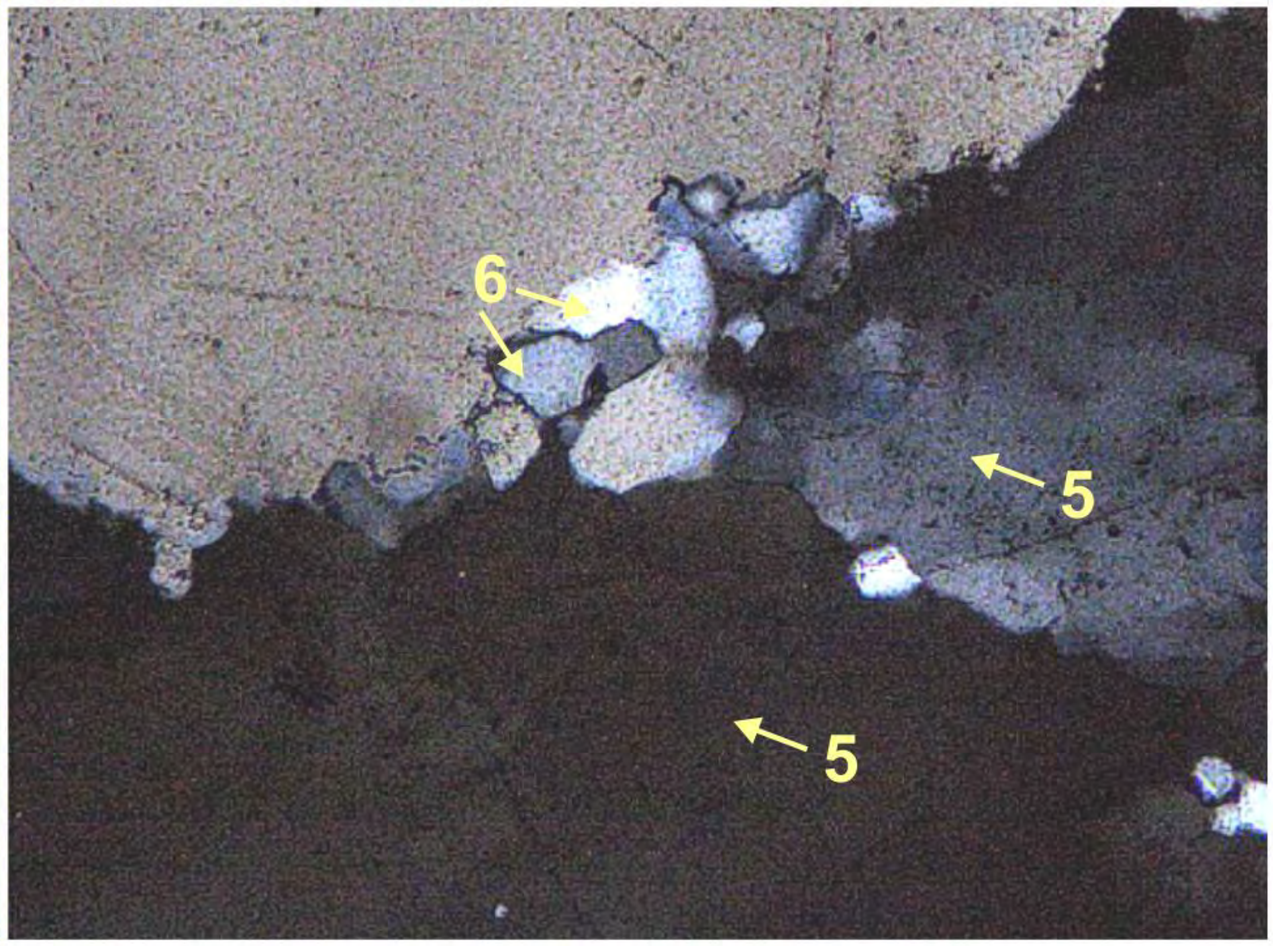
6
5
5

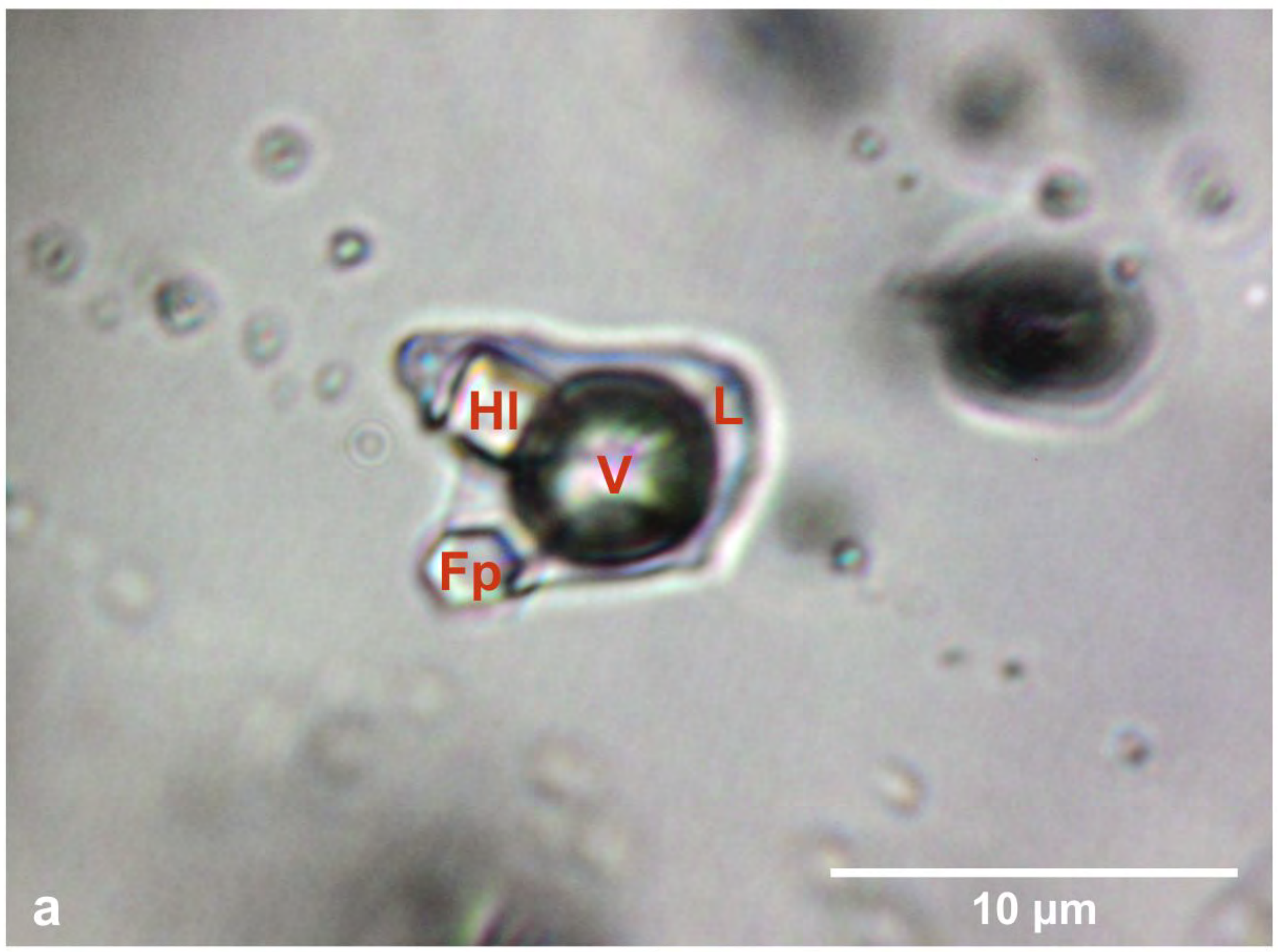
HI
L
V
Fp
10 µm
a

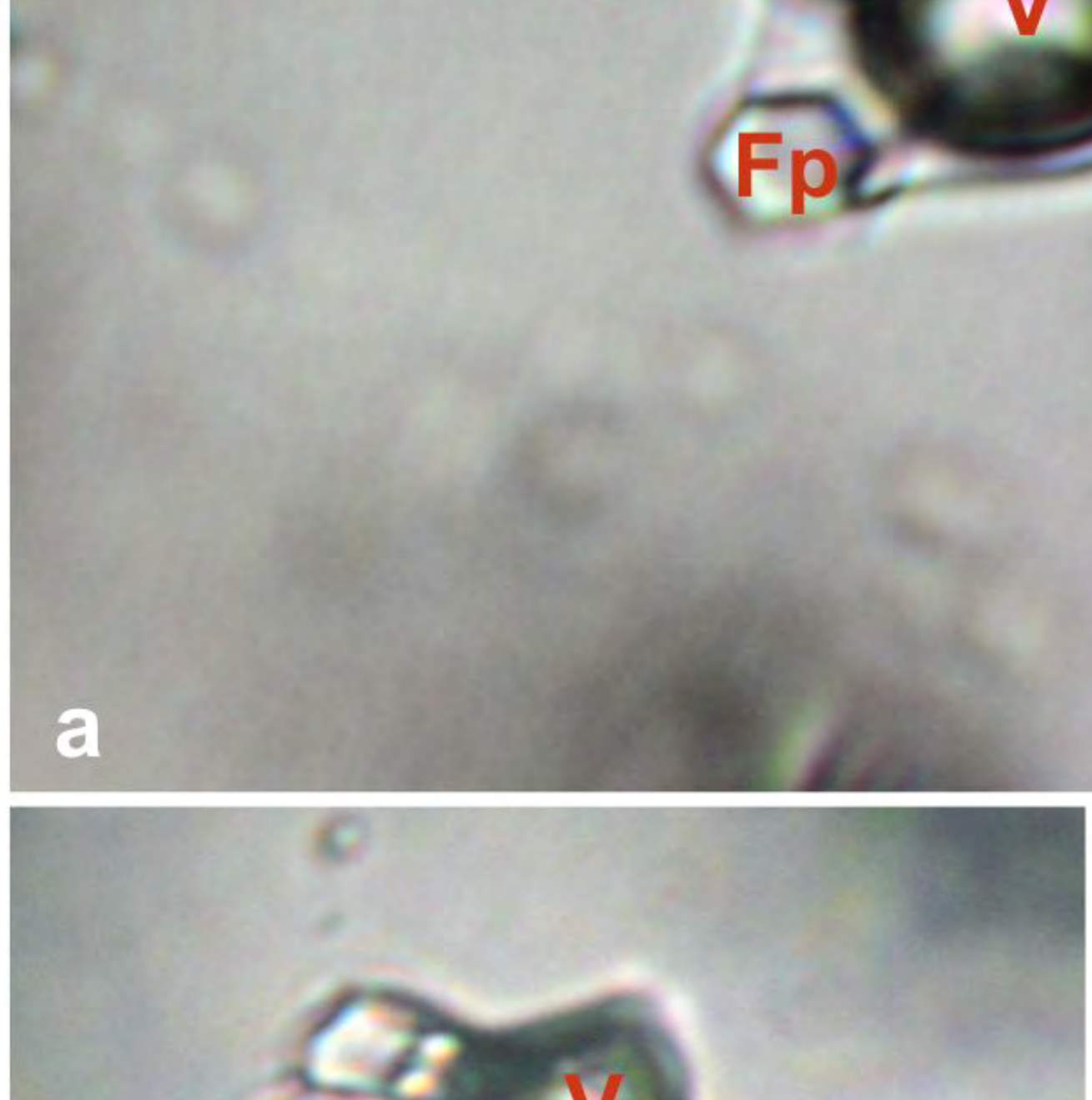
V
Fp
HI
Syl
L
Hem
10 µm
b

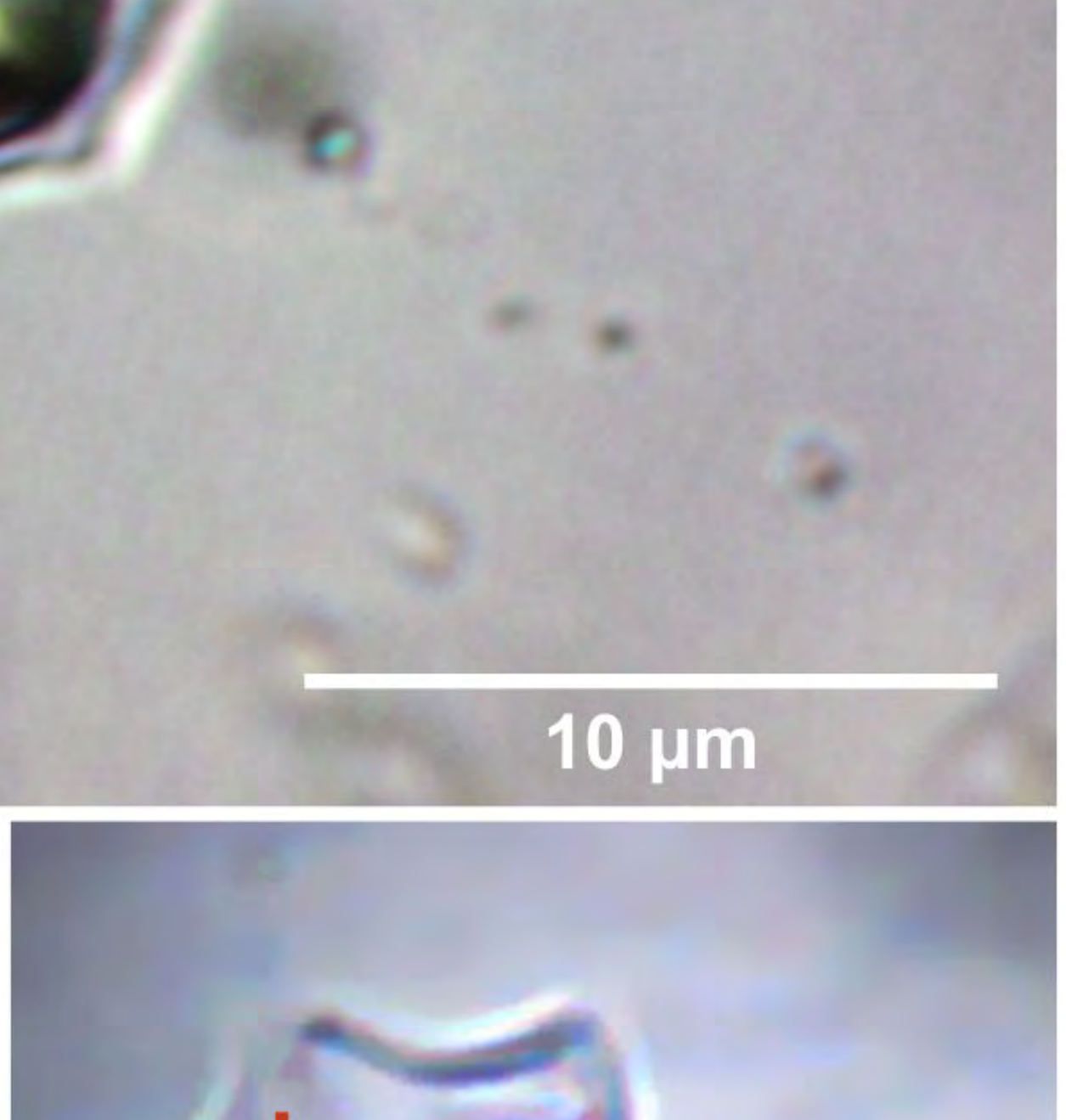
L
HI
Amp
Syl
V
Amp
Mag
10 µm
c

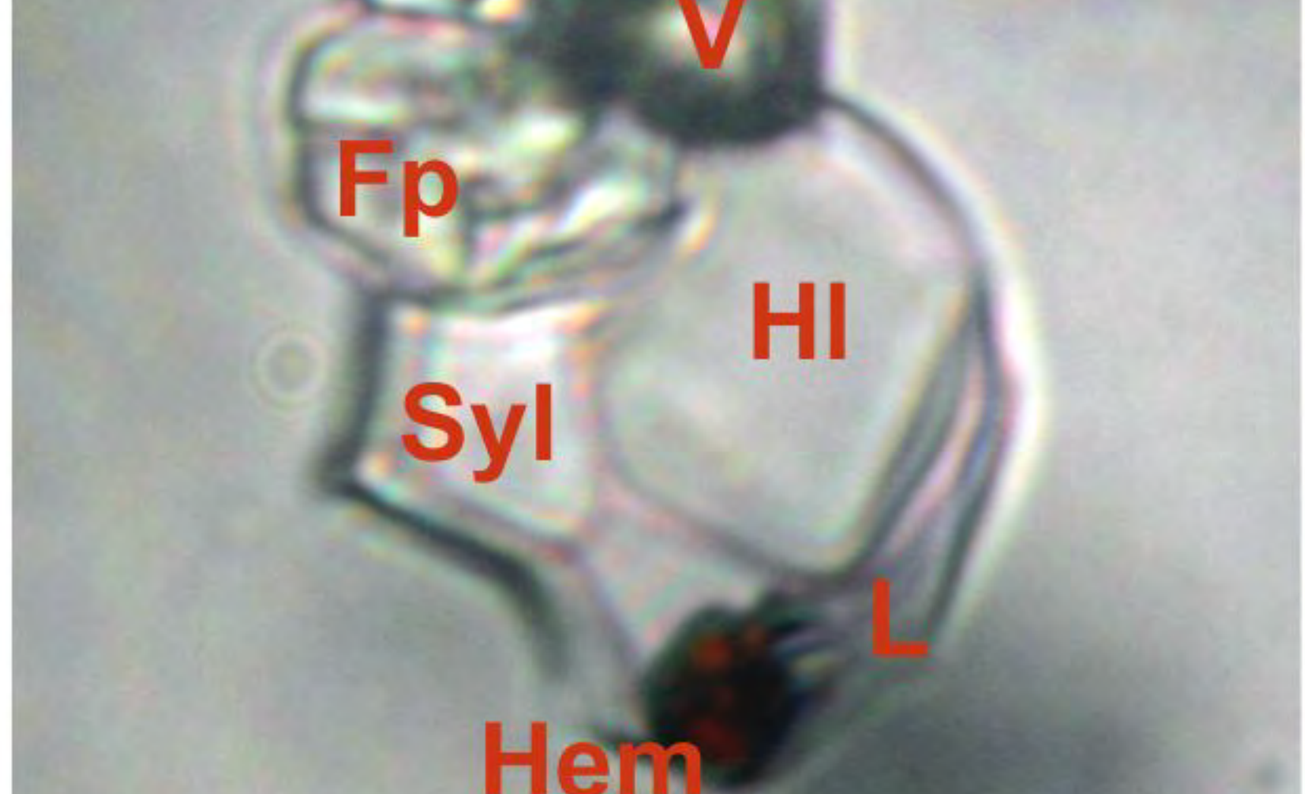
HI
V
Mag
Fp
L
5 µm
d

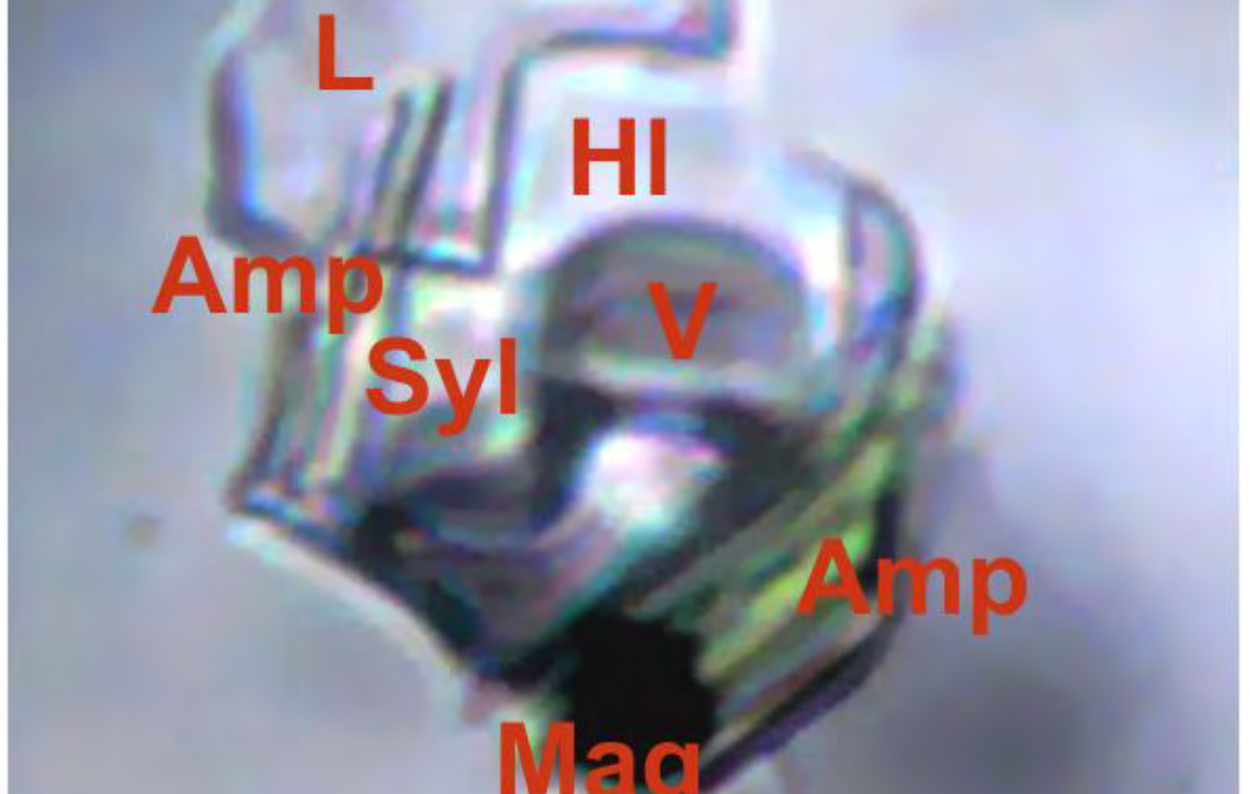
V
Mag
L
HI
Amp
5 µm
e

Late secondary L-V two-phase inclusions

Late secondary V-L two-phase inclusions

Early secondary L-V-DM multiphase inclusions (partial homogenization)

Frequency (n)

0 2 4 6 8 10 12 14

150 200 250 300 350 400 450 500 550 600

a

Homogenization temperature (°C)

Sylvite

Halite

Ferropyrosmalite

Frequency (n)

0 1 2 3 4 5 6 7 8 9

150 200 250 300 350 400 450 500 550 600

b

Melting temperature (°C)

Early secondary L+V±S multiphase inclusions

Early secondary L+V±S multiphase inclusions without halite

Late secondary V-L two-phase inclusions

Late secondary L-V two-phase inclusions

Frequency (n)

0 2 4 6 8 10 12 14 16 18 20

0 5 10 15 20 25 30 35 40 45 50 55 60 65 70 75

c

Salinity (wt. % NaCl eq.)

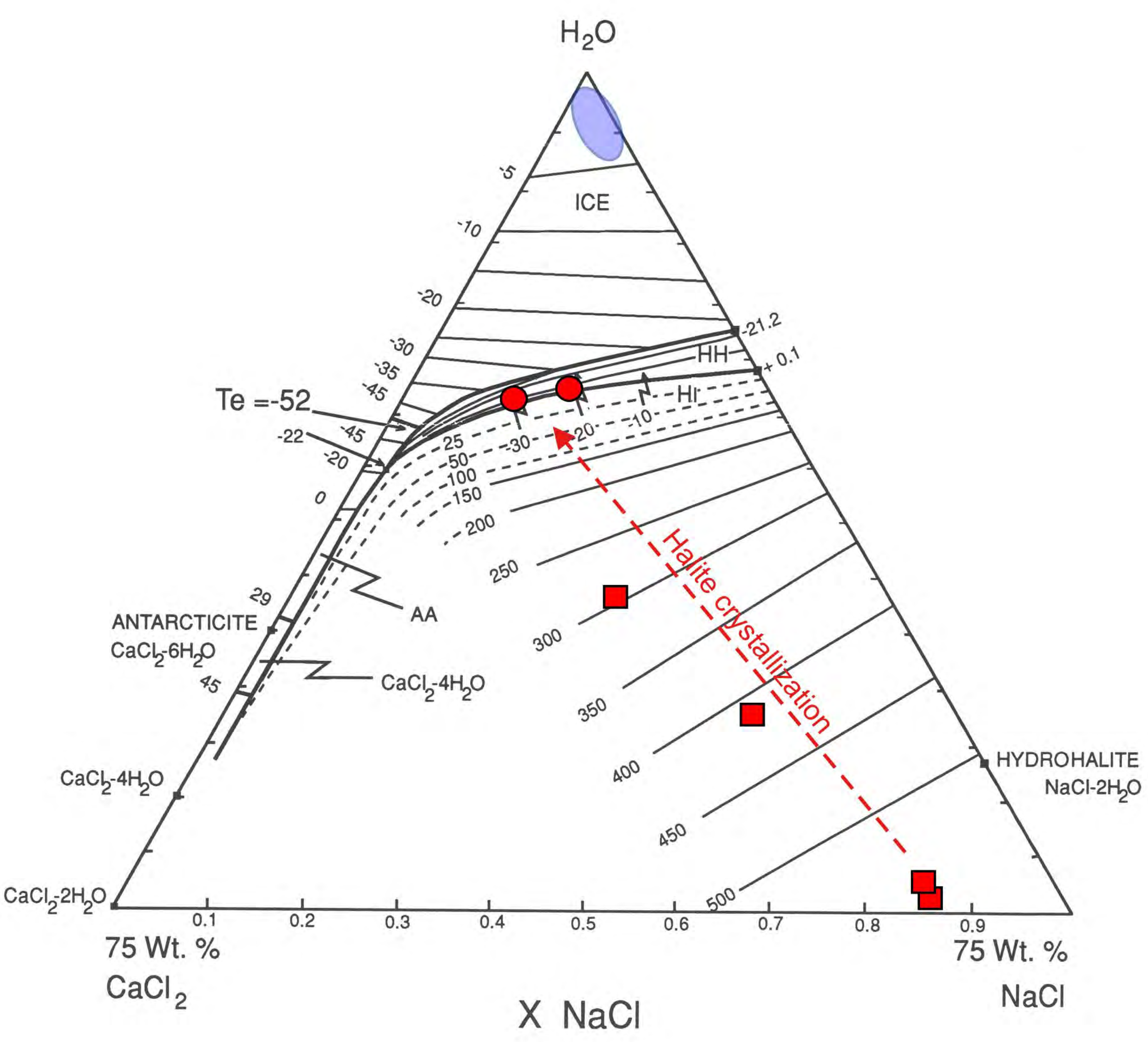
H2O
ICE
-5
-10
-20
-30
-35
-45
-21.2
+ 0.1
HH
HI
Te =-52
-22
-45
-20
0
25
-30
-50
-100
-150
-200
-20
-10
250
300
350
400
450
500
Halite crystallization
29
45
ANTARCTICITE
CaCl2-6H2O
AA
CaCl2-4H2O
CaCl2-4H2O
CaCl2-2H2O
HYDROHALITE
NaCl-2H2O
0.1
0.2
0.3
0.4
0.5
0.6
0.7
0.8
0.9
75 Wt. %
CaCl2
75 Wt. %
NaCl
X NaCl

Natural, non-heated samples

Ferropyrosmalite

Hematite

Heated samples

Chloro-clino-amphibole
(unpolarized)

Water

Clino-amphibole
(polarized)

⊥ c-axis

// c-axis

Magnetite

Intensity (arbitrary units)

Raman shift (cm^{-1})

a

b